technologies

MDPI

Article

Analog Realization of Fractional-Order Skin-Electrode Model for Tetrapolar Bio-Impedance Measurements

Vassilis Alimisis *, Christos Dimas *, Georgios Pappas and Paul P. Sotiriadis *

Department of Electrical and Computer Engineering, National Technical University of Athens, 15780 Athens, Greece; g30pappas@gmail.com

* Correspondence: alimisisv@gmail.com (V.A.); chdim@central.ntua.gr (C.D.); pps@ieee.org (P.P.S.)

Received: 21 September 2020; Accepted: 26 October 2020; Published: 2 November 2020

Abstract: This work compares two design methodologies, emulating both AgCl electrode and skin tissue Cole models for testing and verification of electrical bio-impedance circuits and systems. The models are based on fractional-order elements, are implemented with active components, and capture bio-impedance behaviors up to 10 kHz. Contrary to passive-elements realizations, both architectures using analog filters coupled with adjustable transconductors offer tunability of the fractional capacitors' parameters. The main objective is to build a tunable active integrated circuitry block that is able to approximate the models' behavior and can be utilized as a Subject Under Test (SUT) and electrode equivalent in bio-impedance measurement applications. A tetrapolar impedance setup, typical in bio-impedance measurements, is used to demonstrate the performance and accuracy of the presented architectures via Spectre Monte-Carlo simulation. Circuit and post-layout simulations are carried out in 90-nm CMOS process, using the Cadence IC suite.

Keywords: tetrapolar measurement; bio-impedance; analog integrated circuits; fractional-order models; electrode; skin

1. Introduction

The electrical properties of tissues are strongly related to their structural characteristics and their functional properties [1–3]. Bio-impedance measurements for example provide valuable information about the structural characteristics of a tissue, such as its hardness, as well as about many biological parameters including Blood Pressure (BP), Pulse Transit Time (PPT), Heart Rate (HR), and blood glucose levels [4,5]. In addition, bioimpedance measurements make use of complex, noninvasive, radiation-free diagnostic tools like Electrical Impedance Tomography (EIT) and Electrical Impedance Spectroscopy (EIS), in applications such as ventilation monitoring, brain ischemic hemorrhage detection, neuroimaging, and tumor detection [6,7].

The most common way to perform bio-impedance measurements is by applying a small amplitude alternating current through a pair of conductive electrodes attached on the patient's skin and then by measuring the generated potential. The frequency of the injected current can reach up to several hundreds of kHz, while its amplitude is selected to meet safety standards [4]. The hardware-electrode setup for a single impedance measurement can be bipolar (2 electrodes for both current injection and voltage measurement) or tetrapolar (2 separate electrode pairs for current injection and voltage measurement—also called four-terminal), as depicted in Figure 1 [8–11]. Measuring bio-impedance is a challenging process requiring properly designed instrumentation electronics and measurement methodology. The main design challenges are the sensitivity to strong polarization effects caused by the common injection and measuring path (as is the case in the Bipolar measurement setup) [12] as well as the highly unstable contact impedance of the electrodes which varies with electrode size [13], pressure, humidity, and skin surface condition [14–16]. To address these issues, most bio-impedance measurement systems use the more robust tetrapolar measurement setup (Figure 1 right) [8,17,18].

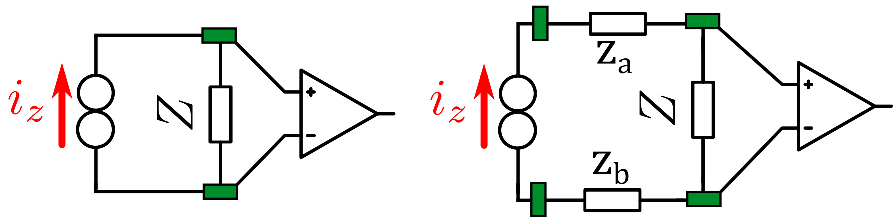

Figure 1. Brief schematic of a bipolar measurement setup (**left**) and a tetrapolar measurement setup (**right**): green rectangles indicate the electrodes placed. Z refers to the impedance under measure, while z_a and z_b refer to the bio-impedances between injection and measurement electrodes. The schematics are based on the description in [11], assuming infinite current source output impedance, infinite instrumentation amplifier input impedance, and negligible electrode impedances.

However, the tetrapolar bio-impedance measurement setup also faces some challenges. The most important is the unpredictable sensitivity distribution near the measuring area [17,19]. The sensitivity values can get locally negative [20], while the phase can be erroneously measured positive on capacitive and resistive domains [17]. Furthermore, common signals in differential measurements usually cause problems, especially if stray capacitances are present and the voltage recording instrumentation circuitry has low Common Mode Rejection Ratio (CMRR) [17,21].

Proper modelling of the tissues under test electrical characteristics is a crucial step during the design process of bio-impedance measurement systems. To this end, designers simulate and employ equivalent circuits of the SUT [21–24], usually implemented using lumped passive elements (capacitors and resistors). By utilizing different values of resistors and capacitors, they can simulate different measurement scenarios and setups in order to both determine the measurement system's specifications and simulate its performance. However, the actual impedance behavior of most tissues is described by the Cole or Debye models [25–27] that present large variations at their parameters [16,26].

Hence, a major limitation of tissue models implemented using passive elements is that they cannot be used for evaluation and calibration of real-world systems as they offer no tunability. Bio-impedance measurement systems often require several months or even years of testing and calibration to provide accurate measurements. To this end, human or animal test subjects are typically employed, significantly increasing the complexity and cost of the development procedure.

In this work, we propose an active, easily tunable circuit implementation of the Cole's skin and electrode models. The design is based on applications from fractional calculus, since fractional-order models offer more degrees of freedom in comparison with integer-order realizations [28–30]. To this end, based on the non-integer exponent parameter of the Cole's equation [25], we propose two tunable fractional-order capacitor implementations, implemented as analog filters (voltage output) with a transfer function H(s). The filters can be transferred to impedances (current output) if a voltage-to-current converter (V/I) is connected at the output stage. By utilizing the actively implemented fractional-order capacitors along with an operational transconductance amplifier (OTA)-based tunable resistor, we implement the Cole's model in transistor level. The proposed circuit architecture is intended to be used as an analog front-end and along with the required digital circuits to shape an application-specific integrated circuit (ASIC) for evaluation and calibration of bioimpedance measurement systems. The circuit is designed, laid out, and simulated in Cadence using a Taiwan Semiconductor Manufacturing Company (TSMC) 90-nm CMOS process.

Both electrode and skin Cole IC-design models are validated and compared to the RC approximations (magnitude and phase) for the models' mean parameter values. Moreover, we examine the proposed circuits' adaptability on major variations of the models' parameters. In addition, some tetrapolar measuring setups that include the implemented models are simulated, testing the measured impedance values in various conditions (target's impedance order and shunt resistors' imbalance).

The remainder of this paper is organized as follows. Section 2 describes the electrode and skin Cole theoretical models adopted for this design and the particular selection reasons. The implementation and behavior of the involved models are presented in Section 3 in the TSMC 90-nm CMOS process. Furthermore, in Section 4, validation is performed via simulated tetrapolar measurements on specific target impedances. Finally, Section 5 concludes this work.

2. Skin and Electrode Cole Models

In this section, the skin and electrode Cole models used for the ASIC implementation are briefly presented. The two models are structurally similar containing a resistor (called "gap resistor") in series with a fractional order impedance. In both cases, the fractional order impedance is formed as a parallel combination of a resistor and a fractional capacitor acting as a Constant Phase Element (CPE), introducing the Cole behavior.

2.1. The Skin Model

Many equivalent circuit models have been proposed for the skin tissue complex impedance [31–33]. Among those, we have selected the simplified Cole model [31] to implement in an ASIC form. This is because the Cole model captures tissue behavior with electrodes placed in relatively short distance (usually 2–4 centimeters), and, within a wide frequency range (e.g., 1 Hz–10 kHz) covering multiple bio-signal types. Therefore, this makes the Cole model an attractive candidate for supporting the development of modern wearable applications.

The Cole model of the total skin impedance, including the contact resistor, is expressed as

$$z_{skin}(\omega) = R_{\infty,s} + \frac{R_{0,s} - R_{\infty,s}}{1 + (j\omega)^{a_s} \cdot (R_{0,s} - R_{\infty,s})C_s} \tag{1}$$

where $R_{\infty,s}$ is the contact (gap) resistor and such that $z_{skin}(\infty) = R_{\infty,s}$, $R_{o,s}$ is the low frequency resistor, i.e., $z_{skin}(0) = R_{o,s}$, a_s is the fractional CPE order and C_s is the pseudo-capacitance of the CPE. The skin Cole model is shown in the left side of Figure 2, where the CPE's complex impedance is defined as [31–33]

$$z_{CPE} = \frac{1}{(j\omega)^{a_s} C_s}. \tag{2}$$

Finally, a useful characteristic of the Cole model is its time constant τ_s defined as

$$\tau_s = \sqrt[a_s]{(R_{0,s} - R_{\infty,s})C_s}. \tag{3}$$

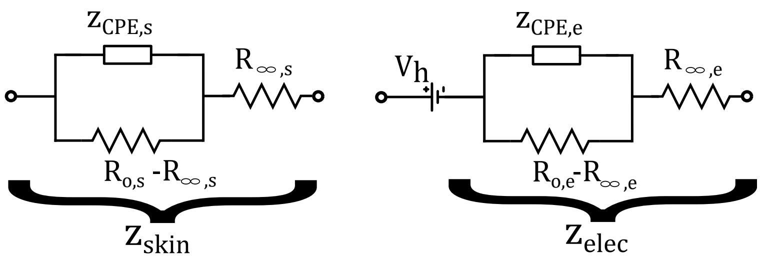

Figure 2. Cole models of the skin (**left**) and electrode (**right**).

For a frequency range of 1 Hz to 10 kHz, typical upper-arm Cole skin model parameters are shown in Table 1, [31]. Table 2 indicates the range of $R_{o,s}$, a_s, and C_s of the Cole skin model for a variety of human body tissues [31–33].

Table 1. Skin (upper arm) and electrode Cole model typical parameter values [16,31].

Parameter	R_∞ **(kΩ)**	R_o **(MΩ)**	τ **(s)**	a	C **(nF/sec^{1-a})**
Skin	1.86	1.39	0.53	0.749	447
Electrode	0.21	1.08	1.41	0.942	1.92

Table 2. Indicative skin and electrode Cole model parameter range [16,31–34].

Parameter	R_o **(MΩ)**	a	C **(nF/sec^{1-a})**
Skin	0.64–1.46	0.63–0.86	61.2–1042.1
Electrode	0.65–2.09	0.8–0.99	1.39–2.09

As mentioned, the presented models and parameters target the frequency range 1 Hz and 10 kHz covering HR, PPT, BR, neuroimaging, and skin impedance measurement applications [4,35]. However, there are other bio-impedance measurement applications outside this frequency range, e.g., lung EIT monitoring functioning at 100 kHz or higher, cancer tissue detection with EIS at about 1 MHz [24,36], etc.

2.2. The Electrode Model

The Cole electrode model has been discussed in many studies and for various electrode sizes and materials [14,15,34]. In bio-impedance and ECG measurements $AgCl$-type electrodes are typically preferred [15]. Moreover, dry electrodes, versus wet (with conductive-gel), are used in long-term monitoring, which is essential for recording the evolution of bio-signals [14] in many modern applications. With these in mind we focus on a Cole model for dry and circular $AgCl$ electrode with a diameter of about 25 mm. Specifically, the electrode Cole model implemented in this work is described in [16] and its impedance is

$$z_{el}(\omega) = R_{\infty,e} + \frac{R_{0,e} - R_{\infty,e}}{1 + (j\omega)^{a_e} \cdot (R_{0,e} - R_{\infty,e})C_e} \tag{4}$$

where $R_{\infty,e}$ is the contact (gap) resistor and such that $z_{el}(\infty) = R_{\infty,e}$, $R_{o,e}$ is the low frequency resistor, i.e., $z_{el}(0) = R_{o,e}$, a_e is the fractional CPE order and C_e is the pseudo-capacitance of the CPE. The time constant τ_e and the complex impedance of the CPE, z_{CPE}, are similar to those of the skin Cole model corresponding to (2) and (3).

The electrode Cole model is shown in the right side of Figure 2. It is structurally identical to that of the Cole skin model, with the exception of a DC potential of about 230–250 mV [34] added in series. For a frequency range of 1 Hz to 10 kHz, typical model parameters are shown in Table 1 and their ranges are shown in Table 2 [16,34].

3. Circuit Realization of the Electrode and Skin Cole Models

There are many different designs and methods for the implementation of fractional-order impedance like that of the Cole models [37–59]. First we focus on the fractional capacitor which is the only "fractional" element of the Cole models as shown in Figure 2. Due to the fact that fractional-order elements are not available as off-the-shelf components, their behavior is typically approximated either using continuous fraction expansion (CFE) and active elements [38–46], or using an RC network [47,48]. In this work we consider two active implementations of the Cole model's fractional-order capacitor, and evaluate their accuracy by comparing them to the Valsa-Vlach RC network approximation [47,48] and the ideal expression (2). The first active implementation is called "versatile" [37] and it is based on the Valsa-Vlach CPE impedance approximation mathematical theory [47,48]; while the second one adopts the "Inverse Follow-the-Leader Feedback (IFLF)" methodology [38–44] based on the CPE impedance using the CFE theory.

The low-frequency resistor R_o is also realized actively with an operational transconductance amplifier (OTA). Hence, in Figure 2, the z_{CPE} and R_o parallel combination is fully active and tunable. Finally, the gap resistor R_∞ is orders of magnitude smaller than R_o and its impact is negligible in lower frequencies. For higher frequency operation, we assume that it is included as an external component.

3.1. Valsa-Vlach Fractional Order Capacitor RC Network Approximation

A circuit realization of the Cole model, and more specifically its fractional-order CPE element, with a single fixed RC network lacks tunability and it cannot be used effectively when the model's parameters change. Therefore, here, the implementation of the fractional-order capacitor with an RC network equivalent is done only to provide a reference along with the theoretical model. The RC network circuitry is depicted in Figure 3 and the simulation results are discussed in Section 3.5. It is noted that the simulations are carried out considering the typical Cole parameter values (Table 1).

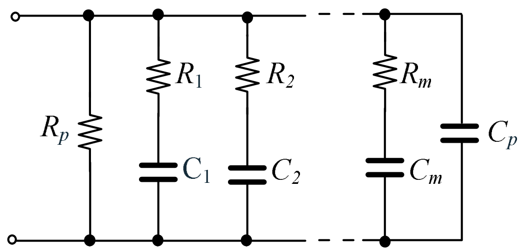

Figure 3. RC network for approximating the behavior of fractional-order capacitors (2) [47].

The general expression of the RC network conductance is given by

$$Y_{tot}(s) = sC_p + \frac{1}{R_p} + \sum_{\kappa=1}^{m} \frac{sC_\kappa}{sR_\kappa C_\kappa + 1}. \tag{5}$$

Following [47,48], the RC network approximation of the CPE is accurate within a certain frequency range $[f_{low}, f_{high}]$ and with a maximum phase error $\Delta\phi$. Selecting the operating range f_{low} = 1 Hz, f_{high} = 10 kHz, and phase tolerance $\Delta\phi$=1.5^o and using the parameters from Table 1, i.e., $a_s = 0.749$ and $C_s = 447nF/sec^{1-a_s}$ for the skin model, and, $a_e = 0.942$ and $C_s = 1.92nF/sec^{1-a_s}$ for the electrode model, we derived the order $m = 5$ (for both models) and the corresponding R and C values as shown in Table 3 using the MATLAB code in [48].

Table 3. Passive element values for approximating the fractional-order capacitors.

Electrode Element	**Value**	**Skin Element**	**Value**
C_1	232.78 pF	C_1	146.63 nF
C_2	203.19 pF	C_2	81.24 nF
C_3	177.37 pF	C_3	45.01 nF
C_4	154.83 pF	C_4	29.94 nF
C_5	135.15 pF	C_5	13.82 nF
C_p	928.34 pF	C_p	17.16 nF
R_1	683.7 MΩ	R_1	1.1 MΩ
R_2	75.2 MΩ	R_2	188.1 kΩ
R_3	8.3 MΩ	R_3	32.6 Ω
R_4	909.4 kΩ	R_4	5.6 kΩ
R_5	100 kΩ	R_5	978.5 Ω
R_p	5.53 GΩ	R_p	5.2 MΩ

3.2. Versatile Active Fractional Capacitor Emulator

To achieve electronic tuning of the CPE's model characteristics we follow [37] and use OTAs and current conveyors of the second generation (CCIIs). Both fractional-order capacitors for skin and electrode models are designed using two cascaded filters, $H_1(s)$ and $H_2(s)$, connected with a multiple-output OTA, which acts as a voltage-to-current (V/I) converter [37–44]. The complete architecture is shown in Figure 4, and the total transfer function, $H(s)$, is given by $H(s) = H_1(s)H_2(s)$.

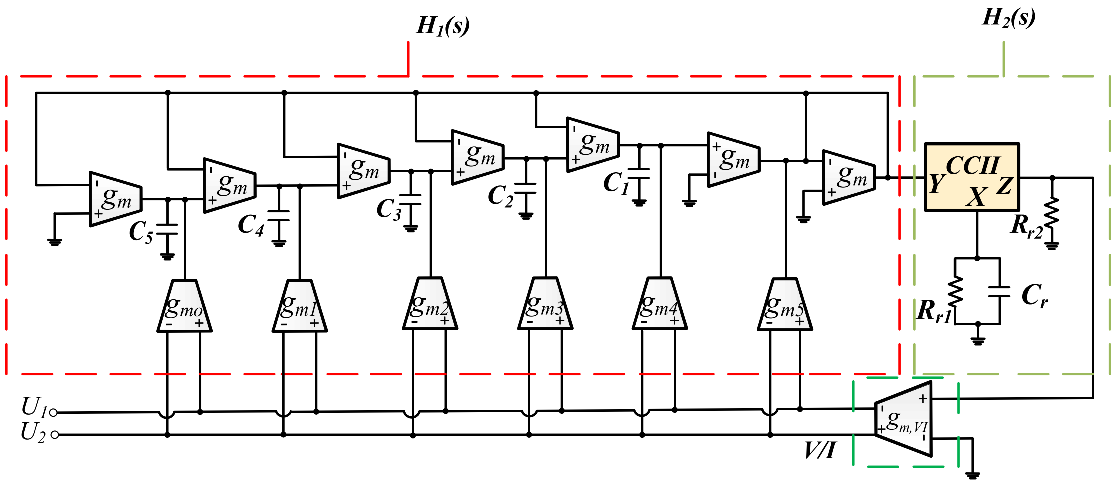

Figure 4. Fractional-order capacitor emulator (versatile methodology) [37].

The differential impedance at the port $U_1 - U_2$ is

$$Z_{cap,approx}(s) = \frac{1}{g_{mvi}H(s)} \tag{6}$$

where g_{mvi} is the transconductance of the V/I converter. The transfer function $H_1(s)$ is that of a 5th order (see Section 3.1) all-pass filter, given by

$$H_1(s) = \frac{A(s)}{B(s)}, \tag{7}$$

where $A(s)$ is

$$A(s) = G_5 s^5 + \frac{G_4 s^4}{\tau_1} + \frac{G_3 s^3}{\tau_1\tau_2} + \frac{G_2 s^2}{\tau_1\tau_2\tau_3} + \frac{G_1 s}{\tau_1\tau_2\tau_3\tau_4} + \frac{G_o}{\tau_1\tau_2\tau_3\tau_4\tau_5} \tag{8}$$

and $B(s)$ is

$$B(s) = s^5 + \frac{s^4}{\tau_1} + \frac{s^3}{\tau_1\tau_2} + \frac{s^2}{\tau_1\tau_2\tau_3} + \frac{s}{\tau_1\tau_2\tau_3\tau_4} + \frac{1}{\tau_1\tau_2\tau_3\tau_4\tau_5} \tag{9}$$

while the transfer function $H_2(s)$ is that of a lossy differentiator

$$H_2(s) = R_{r2}C_r s + \frac{R_{r2}}{R_{r1}}. \tag{10}$$

The schematic of the CCII used for the implementation of $H_2(s)$ is depicted in Figure 5 and the employed OTA schematic is shown in Figure 6 [37,45].

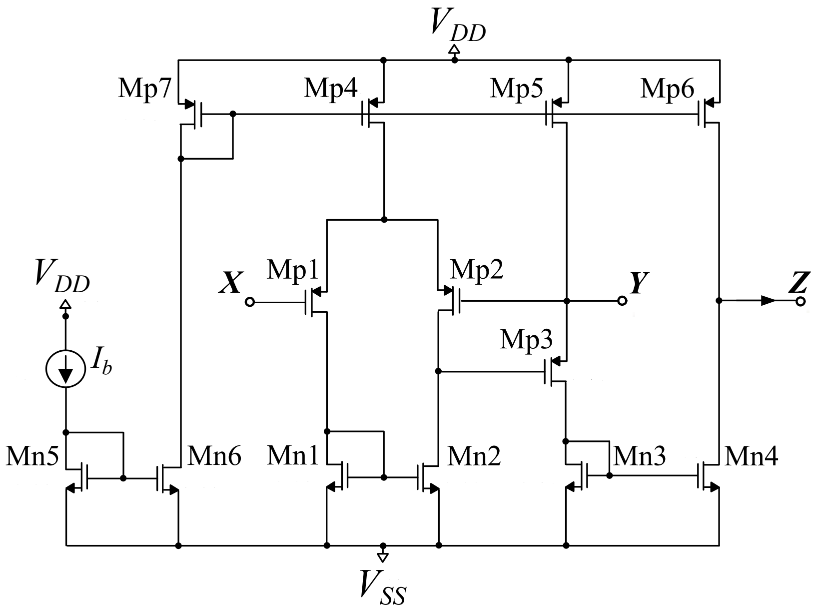

Figure 5. Employed CCII [37].

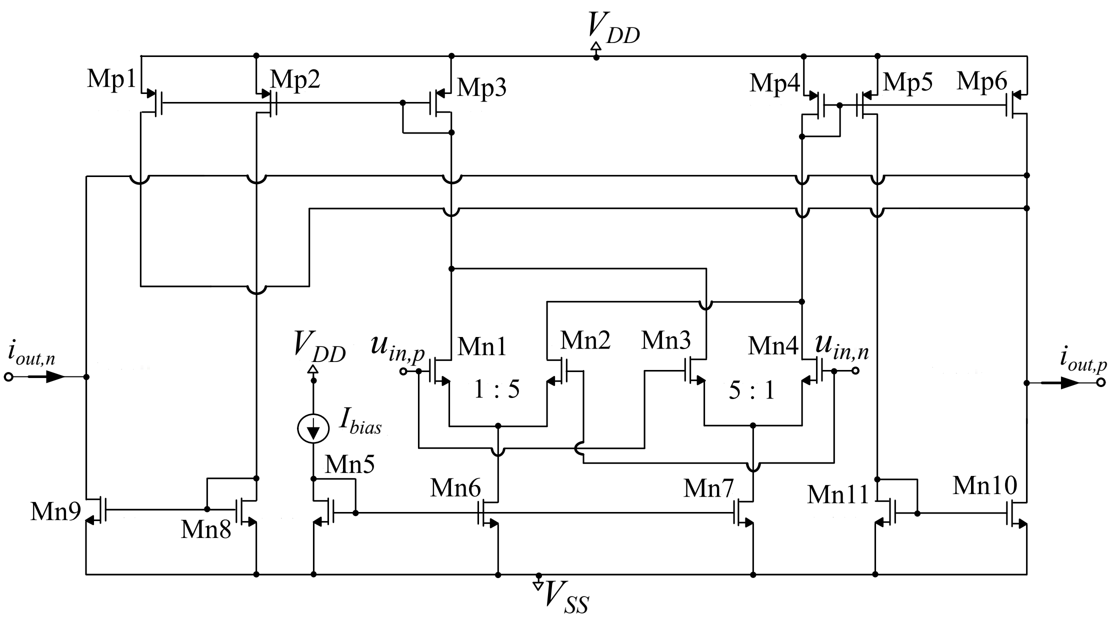

Figure 6. Employed operational transconductance amplifier (OTA) [37,45].

The impedance of the equivalent RC network (derived using MATLAB code) [47,48], which approximates (2) is described by

$$Z_{cap,approx}(s) = \frac{a_5 s^5 + a_4 s^4 + a_3 s^3 + a_2 s^2 + a_1 s + a_o}{b_6 s^6 + b_5 s^5 + b_4 s^4 + b_3 s^3 + b_2 s^2 + b_1 s + b_o}. \quad (11)$$

To implement the fractional-order models, we compare (11) with (6) and choose the value of transcoductance $g_{m,vi}$ to be 100 nS for both models (electrode and skin). All parameters are summarized in Table 4 (derived according to the C and a values in Table 1). The resulting $H(s)$ is expressed by

$$H(s) = \frac{c_6 s^6 + c_5 s^5 + c_4 s^4 + c_3 s^3 + c_2 s^2 + c_1 s + c_o}{d_5 s^5 + d_4 s^4 + d_3 s^3 + d_2 s^2 + d_1 s + d_o}. \quad (12)$$

Table 4. Parameters for the implementation of expression H(s) (12).

Electrode Parameter	Value	Skin Parameter	Value
c_6	1.0	c_6	6.1
c_5	9.393×10^4	c_5	9.388×10^5
c_4	7.715×10^8	c_4	1.221×10^{10}
c_3	6.024×10^{11}	c_3	1.504×10^{13}
c_2	4.464×10^{13}	c_2	1.762×10^{15}
c_1	2.824×10^{14}	c_1	1.836×10^{16}
c_o	1.76×10^{14}	c_o	1.102×10^{16}
d_5	100.0	d_5	33.33
d_4	8.184×10^6	d_4	2.728×10^6
d_3	5.866×10^{10}	d_3	1.955×10^{10}
d_2	3.999×10^{13}	d_2	1.333×10^{13}
d_1	2.593×10^{15}	d_1	8.645×10^{14}
d_o	1.473×10^{16}	d_o	4.910×10^{15}

The presented architecture has been designed in TSMC 90-nm CMOS process, using the Cadence IC design suite. The power supply rails are set to $V_{DD} = -V_{SS} = 0.75$ V, and all transistors operate in the subthreshold region. The transconductance of the corresponding OTA is given by

$$g_m = \frac{5I_{bias}}{9nV_T} \tag{13}$$

where $1 < n < 2$ and $V_T = 26$ mV. Also, the sizes of MOS transistors of the OTA and CCII are summarized in Table 5. The aspect ratio between transistors $M_{n1} - M_{n2}$ and $M_{n3} - M_{n4}$ is equal to 5. We use this multiplicity to increase the linearity of the differential amplifiers pairs and to decrease the transconductance value for the same bias current, compared to an OTA with the same dimensions for the corresponding transistors [60].

Table 5. MOS transistors dimensions—OTA and CCII.

OTA	W/L (μm/μm)	CCII	W/L (μm/μm)
M_{n2}, M_{n3}	2/1	M_{p1}, M_{p2}, M_{p4}	1.6/0.4
M_{n8}– M_9	1/2	M_{p5}, M_{p6}	3.2/0.4
M_{n5}–M_{n7}	0.5/4	M_{p3}	6.4/0.4
M_{n10}–M_{n11}	1/2	M_{n1}-M_{n6}	0.8/0.4
M_{p1}–M_{p6}	10/5	M_{p7}	1.6/0.4
M_{n1}, M_{n4}	0.4/1	–	–

To calculate the factors $G_j = g_{mj}/g_m$ for $j = 0, 1, \ldots, 5$, and the time-constants τ_i for $i = 1, 2, \ldots, 5$, we compare (12) with (7) and (10). The value of transconductance is $g_m = 100$ nS; as a result, the values of the capacitors are calculated by $C_i = \tau_i g_m$ and are summarized in Table 6 for both models. The values of the resistors are $R_{r1} = 142.8$ MΩ ($I_{r1} = 61$ pA) and $R_{r2} = 1.0$ MΩ ($I_{r2} = 52.1$ nA) for the electrode model and $R_{r1} = 156.4$ MΩ ($I_{r1} = 53$ pA) and $R_{r2} = 18.3$ MΩ ($I_{r2} = 2.8$ nA) for the skin model.

The bias current for the implementation of the corresponding transconductance $g_{m,vi} = g_m$ is I_{bias}, which is calculated by the expression $I_{bias} = \frac{9}{5} n V_T g_m$. The current for a transconductance of $g_{mj} = G_j g_m$ can be calculated by $I_{bias,j} = G_j I_{bias}$, where $j = 0, 1, \ldots, 5$ and $I_{bias} = 404$ pA. Adjusting the bias current we can achieve different values for both impedances and the order of the CPE element. The bias current of CCII is $I_b = 20$ nA. The values of the resulting scaling factors are summarized in Table 7 for both models.

Table 6. Values of the capacitors of Figure 4.

Element	Value	Element	Value
C_1	1.22 pF	C_2	13.95 pF
C_3	146.67 pF	C_4	1.54 nF
C_5	17.60 nF	C_r	10.0 nF

Table 7. Values of the scaling factors G_j.

Electrode Model Scaling Factor	Value	Skin Model Scaling Factor	Value
G_o	1.707	G_o	19.188
G_1	1.705	G_1	11.080
G_2	1.505	G_2	6.167
G_3	1.315	G_3	3.418
G_4	1.148	G_4	1.881
G_5	1.000	G_5	1.000

3.3. Inverse Follow-the-Leader Feedback Fractional Capacitor Emulator

In this subsection, we present a typical IFLF architecture for implementation of a fractional-order capacitor. Owing to the fact that the frequency span is from 1 Hz to 10 kHz, the employment of the 5th-order Continued Fraction Expansion (CFE) approximation is a satisfactory solution in order to achieve appropriate results [38–45]. The expression of the 5th-order CFE approximation is described by

$$(\tau s)^{\alpha} \approx \frac{a_5 s^5 + a_4 s^4 + a_3 s^3 + a_2 s^2 + a_1 s + a_o}{b_5 s^5 + b_4 s^4 + b_3 s^3 + b_2 s^2 + b_1 s + b_o} \tag{14}$$

where

$$\begin{aligned}
\alpha_5 = b_o &= -\alpha^5 - 15\alpha^4 - 85\alpha^3 - 225\alpha^2 - 274\alpha - 120, \\
\alpha_4 = b_1 &= 5\alpha^5 + 45\alpha^4 + 5\alpha^3 - 1005\alpha^2 - 3250\alpha - 3000, \\
\alpha_3 = b_2 &= -10\alpha^5 - 30\alpha^4 + 410\alpha^3 + 1230\alpha^2 - 4000\alpha - 12000, \\
\alpha_2 = b_3 &= 10\alpha^5 - 30\alpha^4 - 410\alpha^3 + 1230\alpha^2 + 4000\alpha - 12000, \\
\alpha_1 = b_4 &= -5\alpha^5 + 45\alpha^4 + 5\alpha^3 - 1005\alpha^2 + 3250\alpha - 3000, \\
\alpha_o = b_5 &= \alpha^5 - 15\alpha^4 + 85\alpha^3 - 225\alpha^2 + 274\alpha - 120,
\end{aligned}$$

and α are the order of fractional-order differentiator (all-pass filter) [38–45].

To obtain the tunability of both impedance and order of the element, operational transconductance amplifiers (OTAs) are utilized to implement fractional-order capacitors. Fractional-order capacitor is designed using an all-pass filter, connected with a multiple-output OTA, which acts as a voltage-to-current (V/I) converter [37–44]. The all-pass filter has a transfer function $H(s)$. The complete architecture is shown in Figure 7. The impedance of fractional-order capacitor is given by

$$Z_{cap,approx}(s) = \frac{1}{g_{mvi} H(s)} \tag{15}$$

where g_{mvi} is the transconductance of the V/I converter.

The transfer function $H(s)$ is that of a 5th order all-pass filter, given by

$$H(s) = \frac{A(s)}{B(s)} \tag{16}$$

where $A(s)$ is

$$A(s) = G_5 s^5 + \frac{G_4 s^4}{\tau_1} + \frac{G_3 s^3}{\tau_1 \tau_2} + \frac{G_2 s^2}{\tau_1 \tau_2 \tau_3} + \frac{G_1 s}{\tau_1 \tau_2 \tau_3 \tau_4} + \frac{G_o}{\tau_1 \tau_2 \tau_3 \tau_4 \tau_5} \tag{17}$$

and $B(s)$ is

$$B(s) = s^5 + \frac{s^4}{\tau_1} + \frac{s^3}{\tau_1\tau_2} + \frac{s^2}{\tau_1\tau_2\tau_3} + \frac{s}{\tau_1\tau_2\tau_3\tau_4} + \frac{1}{\tau_1\tau_2\tau_3\tau_4\tau_5}. \tag{18}$$

The IFLF architecture has also been designed in TSMC 90-nm CMOS process, using the Cadence IC design suite. The power supply rails are set to $V_{DD} = -V_{SS} = 0.75V$, and all transistors operate in the subthreshold region. The dimensions of the OTA's MOS transistors are summarized in Table 5 also (we use the same OTA as in versatile design methodology).

To calculate the values of scaling factors $G_j = g_{mj}/g_{mx}$, where $j = 0, 1, \ldots, 5$, $x = a, b, c, d, e, f$ and time-constants τ_i, we compare (16) with (14). The value of the transconductance of electrode's fractional-order capacitor is $g_{mvi} = g_{mx} = 830.2$ nS for all x. As a result, the values of capacitors are calculated by $C_i = \tau_i g_m$ and are summarized in Table 8 for both models. The values of transconductances for the skin's fractional-order capacitor are summarized in Table 9. The resulting scaling factors' values are summarized in Table 10 for both models. It is noted that, like in versatile implementation, these values are derived according to the typical pseudo-capacitor values shown in Table 1.

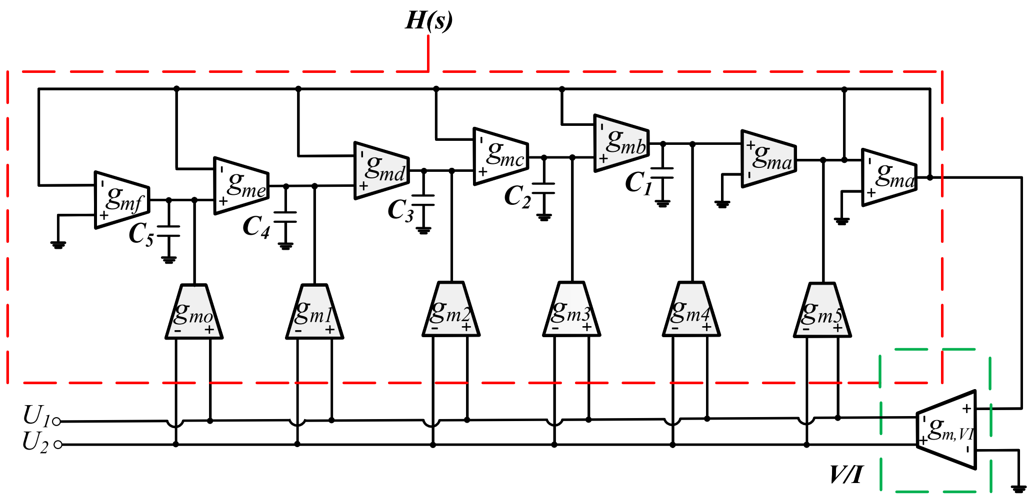

Figure 7. Realization of fractional-order capacitor emulator (Inverse Follow-the-Leader Feedback (IFLF) methodology).

Table 8. Values of the capacitors of Figure 7.

Element	Value	Element	Value
C_1	2.58 pF	C_2	141.43 pF
C_3	689.82 pF	C_4	2.75 nF
C_5	13.80 nF	-	-

Table 9. Values of transcoductance for the skin model of Figure 7.

Parameter	Value	Parameter	Value
g_{ma}	184.84 nS	g_{mb}	674.02 nS
g_{mc}	721.35 nS	g_{md}	729.19 nS
g_{me}	713.18 nS	g_{mf}	564.15 nS
g_{mvi}	55.37 µS	-	-

Table 10. Values of the scaling factors G_j.

Electrode Model Scaling Factor	Value	Skin Model Scaling Factor	Value
G_0	0.002	G_0	0.02
G_1	0.12	G_1	0.19
G_2	0.52	G_2	0.600
G_3	1.92	G_3	1.66
G_4	8.61	G_4	5.33
G_5	422.02	G_5	50.01

3.4. Cole Model Tunable Resistor R_o Realization

In order to achieve tunability of the resistor R_o demonstrated in Figure 2, we use the same multiple OTA (with the same dimensions as shown in Table 5) utilized in the previously presented CPE's design methodologies (Figure 6), since we can achieve the desired transconductance by selecting applicable DC bias current values. Configuration of the programmable OTA as a resistor is depicted in Figure 8 [37,45].

All transistors are biased in the subthreshold region, and so the impedance of the effective resistance is given by

$$R_o = \frac{1}{g_{mo}} \tag{19}$$

where g_{mo} is obtained by (13).

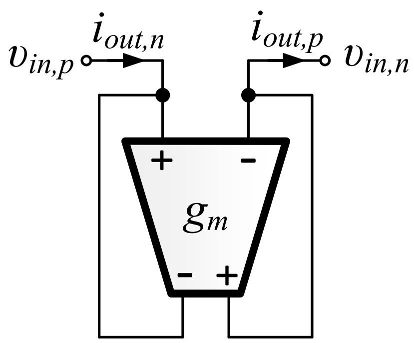

Figure 8. Implementation of tunable resistor emulator [37,45].

Due to the relatively small values of R_∞ for both the skin and electrode models and regarding impedance of the employed OTA being unable to practically achieve values less than 400 kΩ, we have replaced R_∞ with passive tunable resistors (potentiometers). We also note that all the remaining resistors (R_o, R_{r1}, and R_{r2}) used below, are implemented exclusively by programmable OTAs. Therefore, all the model's parameters are implemented actively in IC design except of R_∞.

3.5. Cole Model Circuit Realization Simulation Results

The layout design of the fractional-order skin and electrode models using IFLF design methodology is demonstrated in Figure 9, where the area is 78 µm×278 µm. The layout design of the fractional-order skin and electrode models using versatile design methodology is demonstrated in Figure 10, where the area is 78 µm×329 µm. Both layouts include all elements except capacitors C_i, $i = 1, 2, \ldots, 5$ and resistor R_∞ (potentiometer resistor). All results are from post-layout simulations.

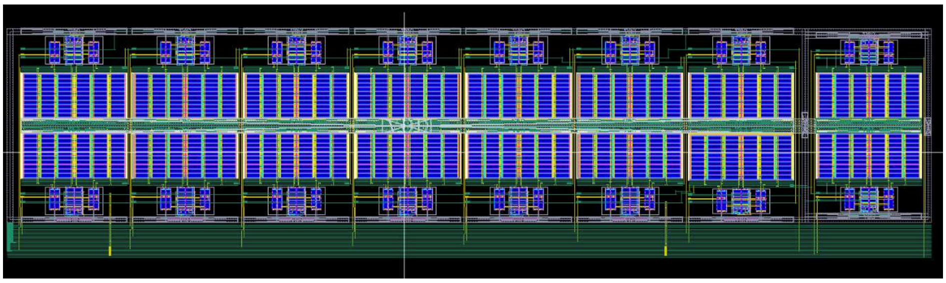

Figure 9. Layout of the implemented fractional-order skin and electrode models (IFLF methodology).

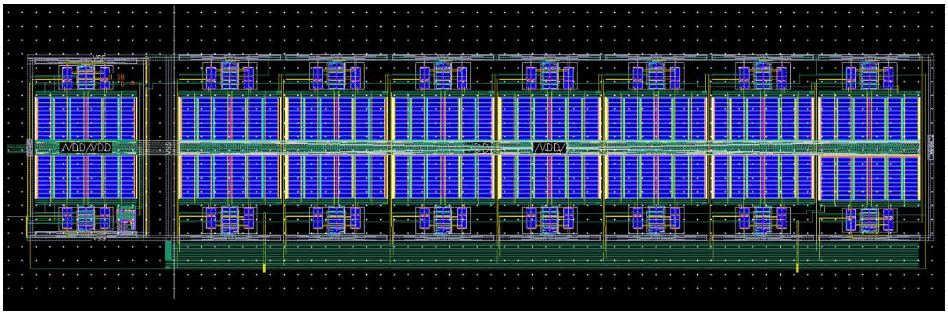

Figure 10. Layout of the implemented fractional-order skin and electrode models (versatile methodology).

The magnitude and phase response for all design methodologies along with that of the ideal RC approximation and that of the theoretically predicted ones are plotted in Figure 11 for the fractional-order electrode model capacitor. The magnitude values are in fine agreement with the theoretical ones. The phase response, which is very important for simulation of the fractional-order capacitor, is also close to the ideal value of $-84.78°$, for a big part of the frequency band. However, the IFLF approach has an error up to 4.5° at the span's boundaries (1 Hz and 10 kHz), while the maximum error of the versatile methodology is at 1.5°.

The corresponding responses of the fractional-order skin model capacitor are shown in Figure 12. As in the electrode's CPE case, the magnitude response shows very low error, especially for the versatile approach (the IFLF values have a maximum error of 25 kΩ at 1 Hz; however, this is minimized at higher frequencies). The phase response, for the case of skin CPE, shows also minimum error in the middle frequencies (the ideal phase is $-67.41°$), while the IFLF methodology shows critical phase errors at the frequency range's limits. At the same time, the versatile methodology provides almost the same results as the ideal RC network simulation.

The obtained impedance responses of the electrode and skin models along with the theoretically predicted ones and that of the ideal RC network approximation are provided in Figures 13 and 14, respectively. It is observed that both approaches result in successful approximations with low average errors. In specific, superior accuracy is obtained in the skin's and electrode's impedance magnitudes (for both the capacitor and the whole Cole models), as shown in Figures 11–13 and Figure 14 (left subfigures). In addition, the models realized with the IFLF topology present low phase error between 10 Hz and 1kHz, but it deviates near the frequency range's limits. However, the IFLF mean and maximum phase errors are lower than those in the corresponding CPE model. In contrast, the versatile design methodology-implemented models have better accuracy near 1 Hz–10 Hz and 1 kHz–10 kHz; however, they present minor errors in the middle frequencies.

As mentioned before, the two design methodologies (versatile and IFLF) approximate the behavior of the fractional order elements. The errors between these two techniques and the theoretical values arise from the approximation's order (CFE and RC approximation). In order to minimize them, the complexity (order) of the whole topology needs to be increased. This is not desirable.

Nevertheless, both methodologies are characterized not only by tunability of impedance and order but also by capability to change the central frequency, which can contribute to minimizing the errors at the boundaries if performed properly (by tuning bias current).

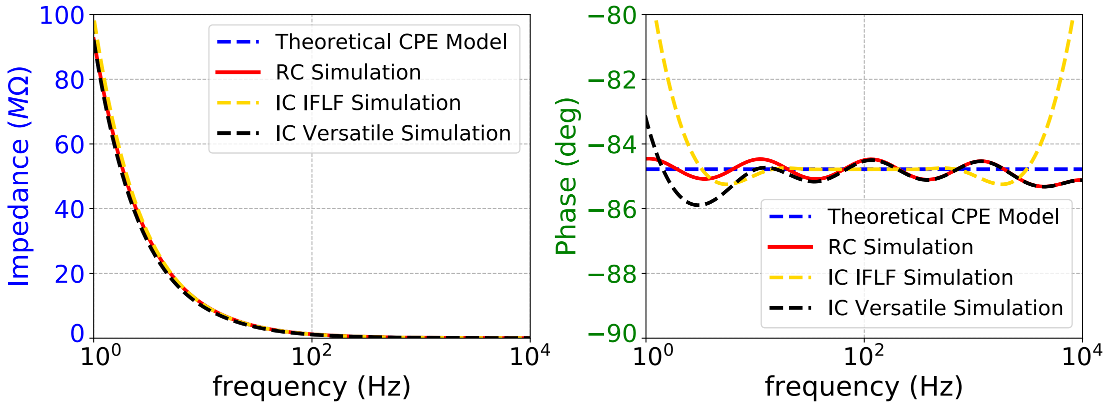

Figure 11. Impedance magnitude (**left**) and phase response (**right**) of the fractional-order capacitor for the case of electrode model.

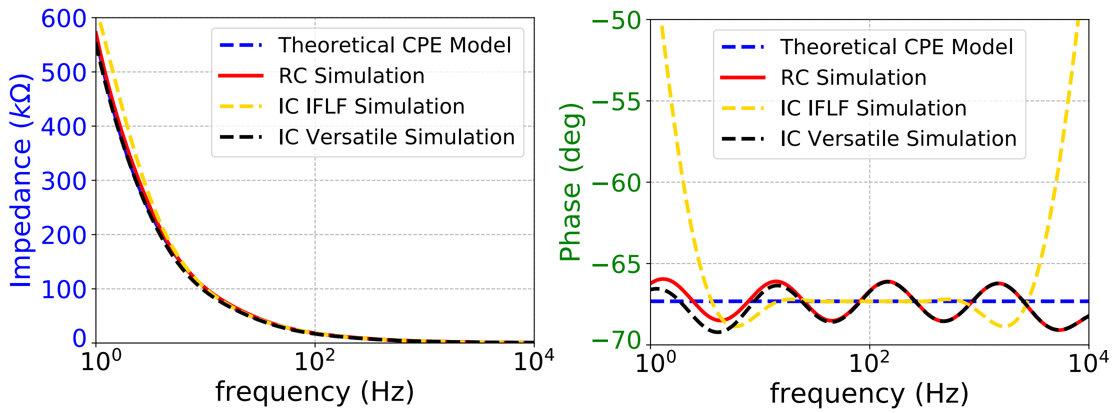

Figure 12. Impedance magnitude (**left**) and phase response (**right**) of the fractional-order capacitor for the case of skin model.

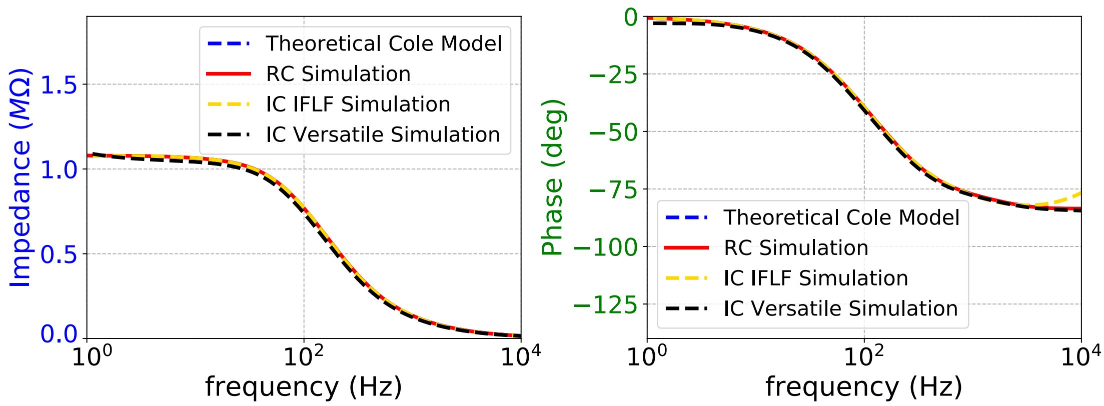

Figure 13. Impedance magnitude (**left**) and phase response (**right**) of fractional-order electrode model.

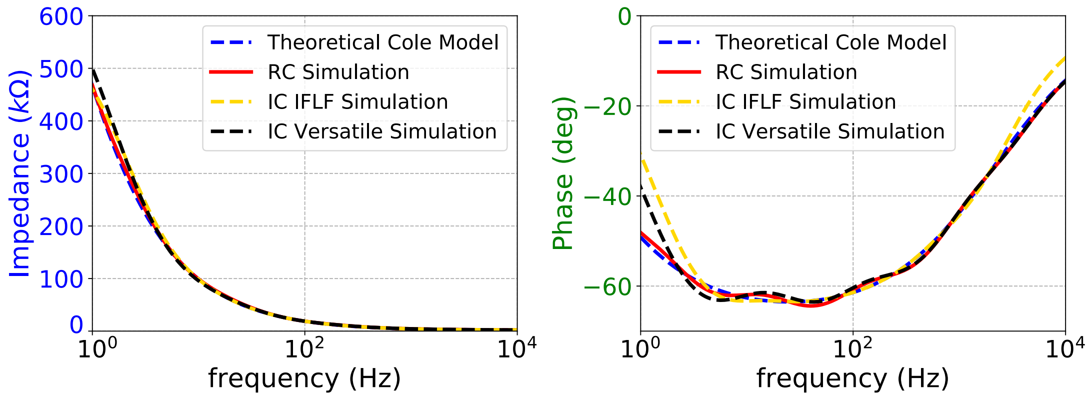

Figure 14. Impedance magnitude (**left**) and phase response (**right**) of fractional-order skin model.

3.6. Cole Models Parameters Variation and Circuit Emulator Trimming

In the previous subsection, we presented the simulation results of RC approximation, and versatile and IFLF design methodologies for both fractional-order skin and electrode models. The parameter values utilized for the models refer to the typical values according to [16,31]. However, these parameters exhibit great variations across different human subjects and are affected by situations such as humidity, pressure, and temperature at the skin-electrode's surface [16,26,31]. In order to implement these possible cases, we have to use a realization methodology which provides tunability and high performance. The RC network provides high performance for a single case, as shown in the previous subsection, but it is not appropriate for examining multiple conditions. The main reason for this drawback is the absence of tunability in passive elements (in order to achieve different cases, we have to continuously change the RC values of the network in Figure 3).

On the other hand, the IC design methodologies offer the possibility to achieve different parameter values. Hence, both architectures (versatile and IFLF) can describe the behavior of both electrode and skin models under various situations by using a single core. In this subsection, we evaluate the performance and accuracy of the presented design techniques in describing different conditions.

3.6.1. Electrode Model Parameter Variation

In this part, we examine the discussed IC methodologies' accuracy for 8 different model cases. The C_e (CPE) and $R_{o,e}$ (low frequency resistor) parameter variations were extracted from trials over human subjects (experimental results) under two conditions (pressure and removing pressure) in [16]. The order of the CPE is assumed $a_e = 0.942$ for all the cases. The selection of appropriate values was derived by adjusting the observed variations around the typical values in Table 1, and they are summarized in Table 11. The minimum and maximum values for the fractional-order capacitor were computed at 1.39 nF/sec^{1-a} and 2.09 nF/sec^{1-a}, respectively, while the corresponding values for $R_{o,e}$ are 650 kΩ and 2.09 MΩ. The high-frequency resistor ($R_{\infty,e}$) values are kept constant at 210 Ω. The cases described are obtained by controlling the transconductance g_{mvi} of the V/I converter and the g_{mo} of the $R_{o,e}$ effective resistor. According to (13), the desired g_{mvi} and g_{mo} can be achieved just by tuning DC bias current (I_{bias}).

Table 11. Electrode Cole parameters values for different cases, $a_e = 0.942$.

Case/Parameter	$R_{o,e}$ (MΩ)	C_e (nF/sec^{1-a})
Case I	1.08	1.75
Case II	2.09	1.39
Case III	0.65	1.92
Case IV	1.51	1.92
Case V	0.65	1.75
Case VI	1.51	1.75
Case VII	0.65	2.09
Case VIII	1.51	2.09

The corresponding results for the two IC methodologies are depicted in Figures 15–22. Both architectures provide high accuracy in all the cases, with the exception of the IFLF phase error near 10 kHz (as in the previous section). This performance cannot be possibly achieved by a single RC network, since it lacks tunability.

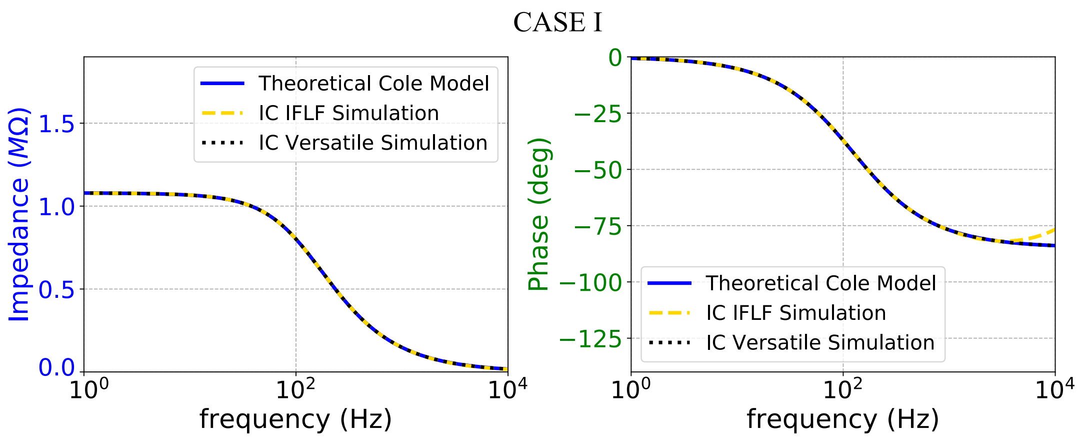

Figure 15. Impedance magnitude (**left**) and phase response (**right**) of the case I fractional-order electrode model.

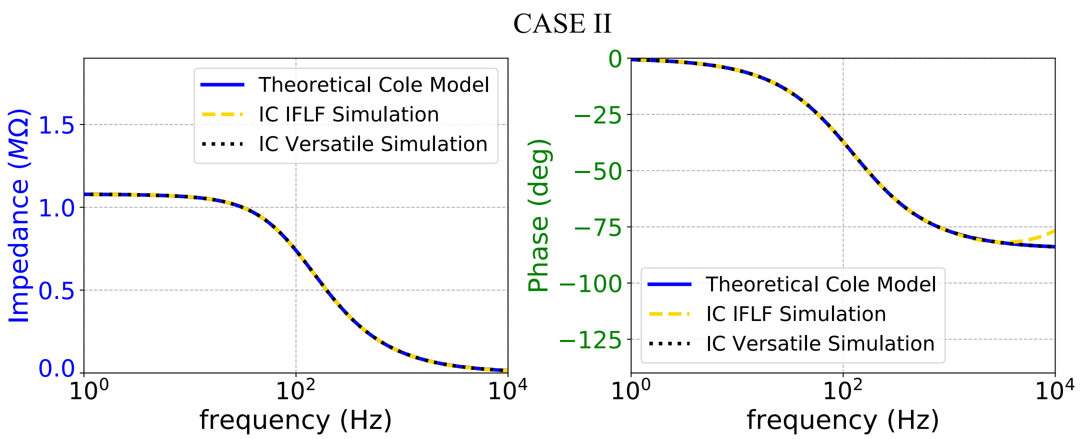

Figure 16. Impedance magnitude (**left**) and phase response (**right**) of the case II fractional-order electrode model.

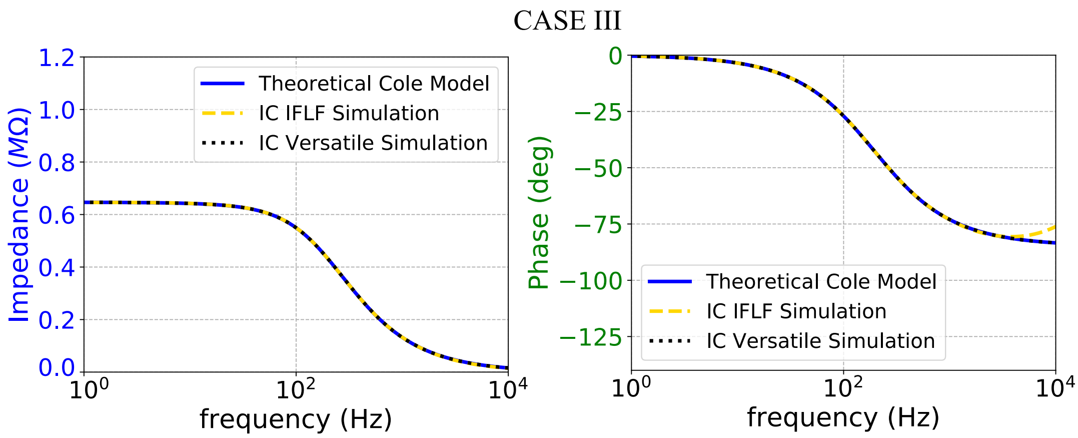

Figure 17. Impedance magnitude (**left**) and phase response (**right**) of the case III fractional-order electrode model.

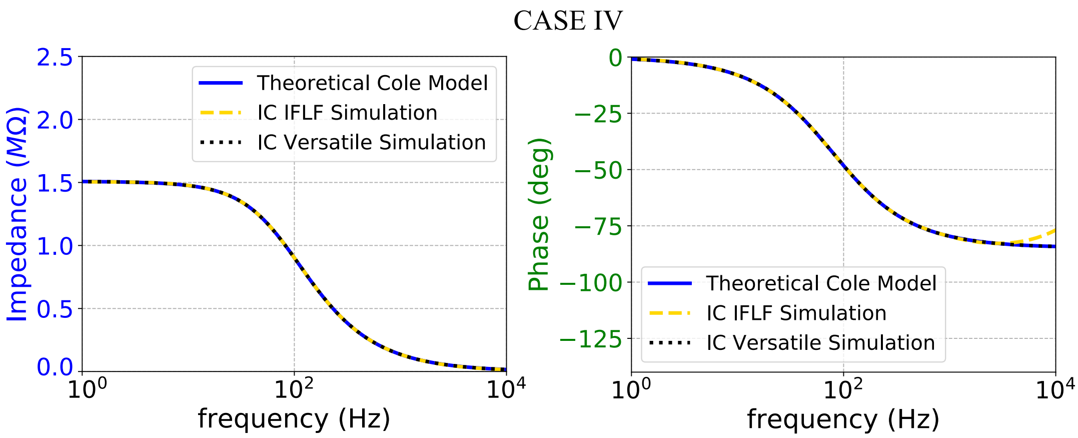

Figure 18. Impedance magnitude (**left**) and phase response (**right**) of the case IV fractional-order electrode model.

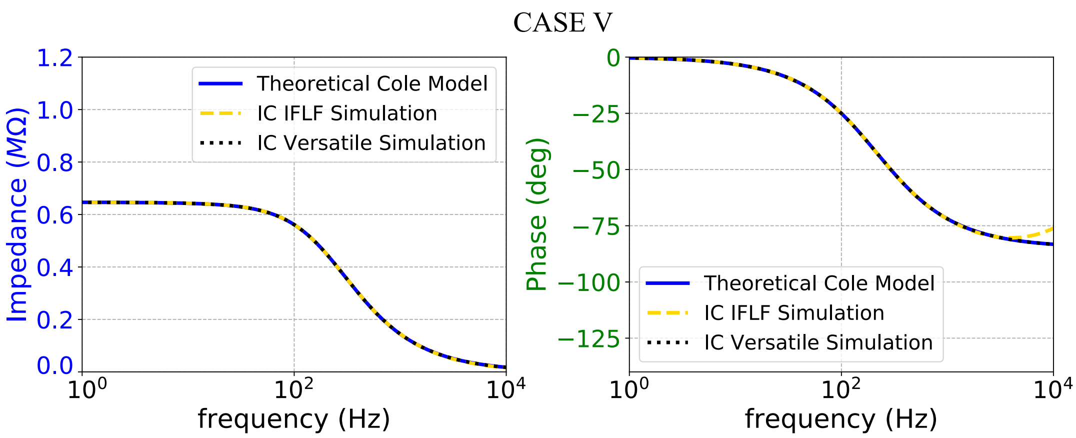

Figure 19. Impedance magnitude (**left**) and phase response (**right**) of the case V fractional-order electrode model.

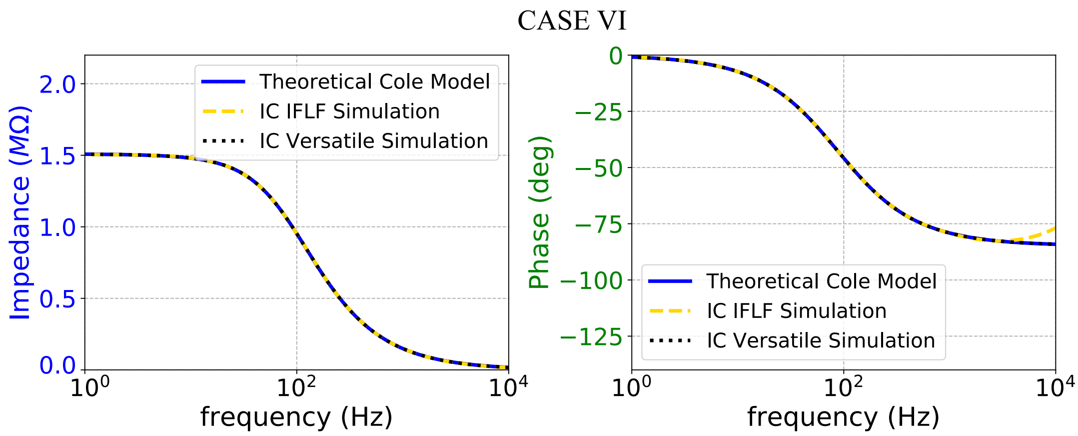

Figure 20. Impedance magnitude (**left**) and phase response (**right**) of the case VI fractional-order electrode model.

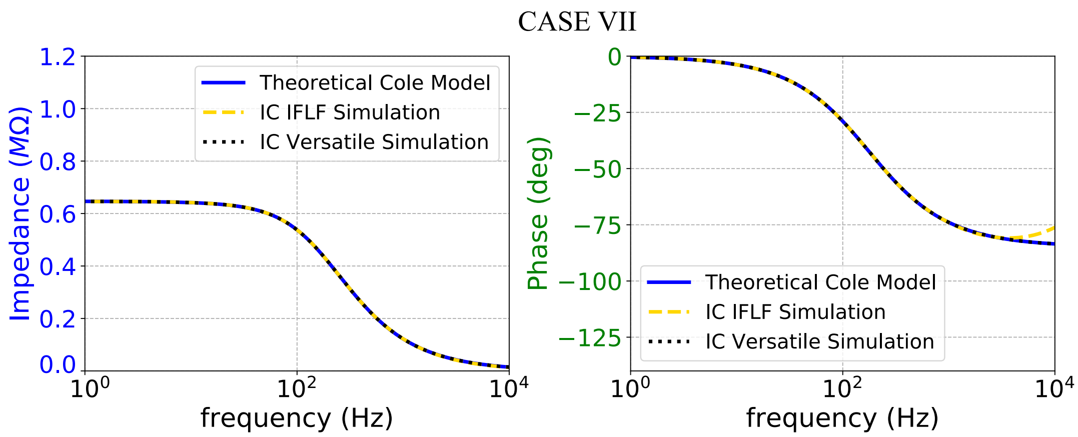

Figure 21. Impedance magnitude (**left**) and phase response (**right**) of the case VII fractional-order electrode model.

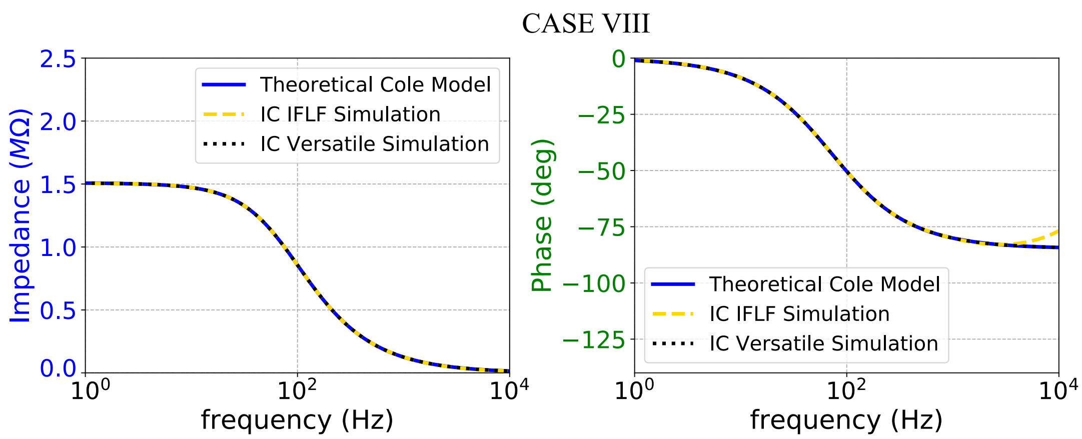

Figure 22. Impedance magnitude (**left**) and phase response (**right**) of the case VIII fractional-order electrode model.

3.6.2. Skin Model Parameter Variation

For the fractional-order skin model, we derived four different cases where C_s and order a_s of the CPE were tuned, according to the values in [26]. The $R_{o,s}$ value was fixed at 1.39 MΩ, and $R_{\infty,s}$ was fixed at 1.86 kΩ (Table 1). The calculated C_s and a_s values are summarized in Table 12. All the above cases are achieved and performed just by adjusting the appropriate DC bias currents (electronic tuning capability). According to (13), we can control the transconductance values g_m, while the values of the capacitors in Figures 4 and 7, as in Tables 6 and 8, are kept constant.

Table 12. Skin Cole parameters values for different cases, $R_{o,s} = 1.39$ MΩ.

Case/Parameter	a_s	C_s **(nF/sec^{1-a})**
Case I	0.86	65.2
Case II	0.81	61.2
Case III	0.82	88.9
Case IV	0.78	73.1

The corresponding results are demonstrated in Figures 23–26, where we approve that the presented architectures provide sufficient accuracy. The results are in fine agreement with the case shown in Figure 14, where the the IFLF phase shows maximum error near the frequency span's limits. It is noted that both designs except for pseudo-capacitance C_s can also achieve order a_s tuning.

CASE I

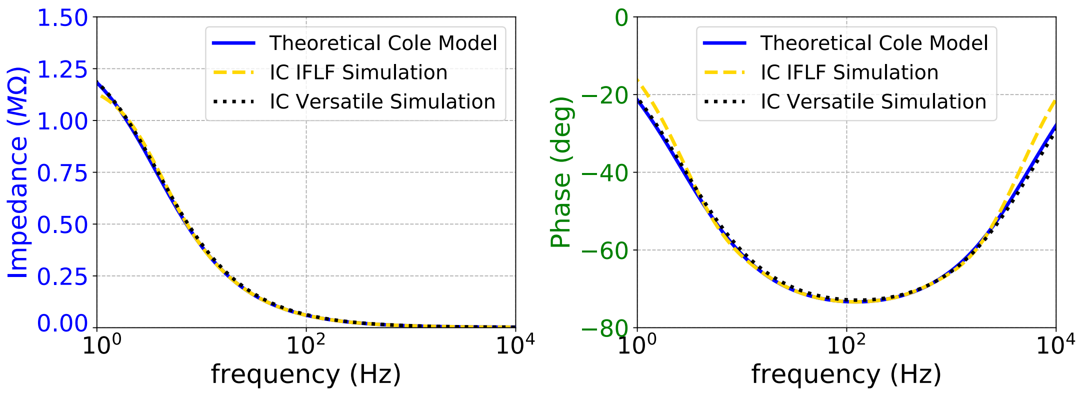

Figure 23. Impedance magnitude (**left**) and phase response (**right**) of the case I fractional-order skin model.

CASE II

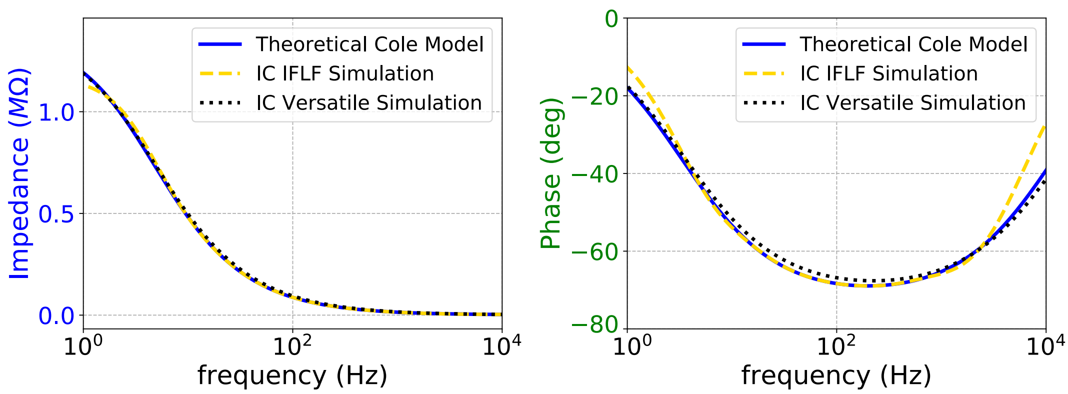

Figure 24. Impedance magnitude (**left**) and phase response (**right**) of the case II fractional-order skin model.

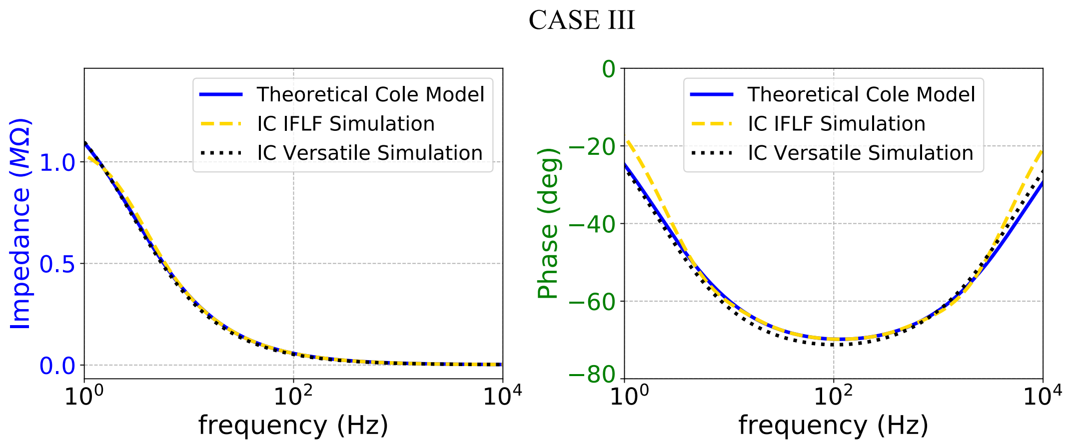

Figure 25. Impedance magnitude (**left**) and phase response (**right**) of the case III fractional-order skin model.

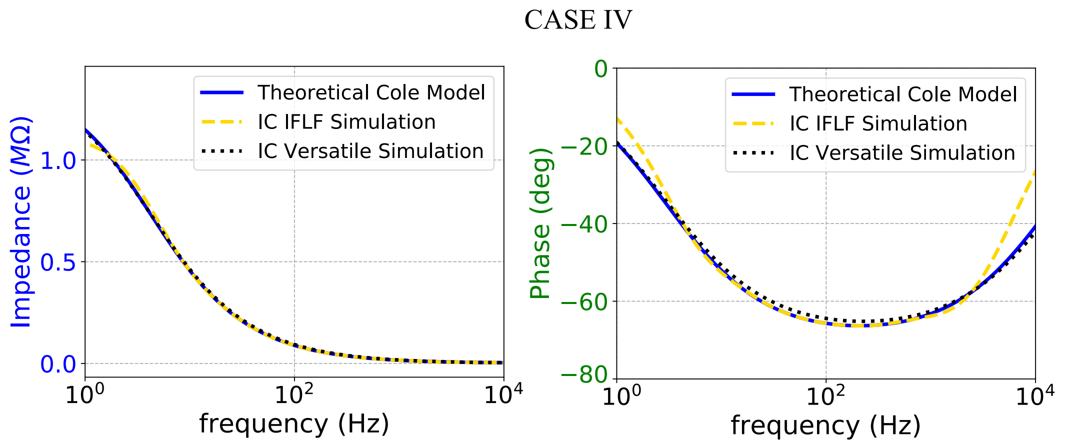

Figure 26. Impedance magnitude (**left**) and phase response (**right**) of the case IV fractional-order skin model.

4. Tetrapolar Model Simulation Results

The models implemented above are utilized in simplified tetrapolar setup test cases in order to observe the impact of electrode and skin impedances at particular bioimpedance measurements. The setup adopted for the tetrapolar AC simulations is shown in Figure 27, assuming 4 vertically placed dry AgCl 2.54 cm (1 inch) diameter electrodes at a distance of 3 cm between each other. We note here that this setup is just indicative; a more realistic representation requires a fine Finite Element (F.E.) forward model, which has to be properly transferred to a complex setup, consisting of blocks based on the presented models.

The two opposite (upper and lower) electrodes inject a 1 mA AC current of frequency between 1 Hz and 10 kHz, while the two middle electrodes perform differential voltage measurement. The electrode material and skin RC equivalent subcircuits are replaced by the fractional integrated IC models, while the extremely sensitive gap impedances of electrodes and skin models (R_∞) are merged in one resistor at each contact, which is manually modified in the simulation. A target impedance, R_b, is placed between the two voltage measurement electodes in parallel with a skin model's RC impedance. R_b is the resistance to be measured in each case. Finally, two 20 pF parasitic capacitors are included for both voltage output traces to include any possible stray capacitive effects [21,22].

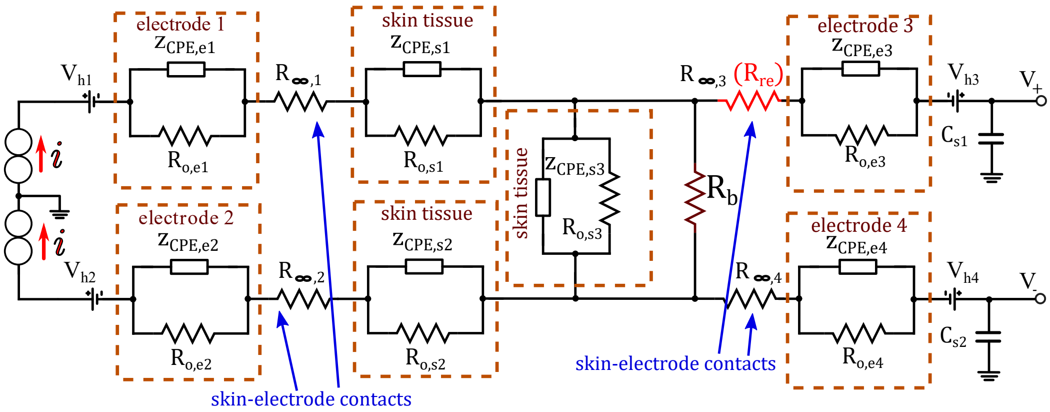

Figure 27. Tetrapolar setup cases.

All simulated AC measurements demonstrate the difference $V_+ - V_-$, as shown in Figure 27, and their magnitude and phase are plotted at a frequency range between 1 Hz and 10 kHz. The layout design of the fractional-order skin and electrode models using IFLF design methodology is demonstrated in Figure 28, where the area is 351 µm×614 µm. The layout design of the fractional-order skin and electrode models using versatile design methodology is demonstrated in Figure 29, where the area is 351 µm×714 µm. Post-layout simulation was performed.

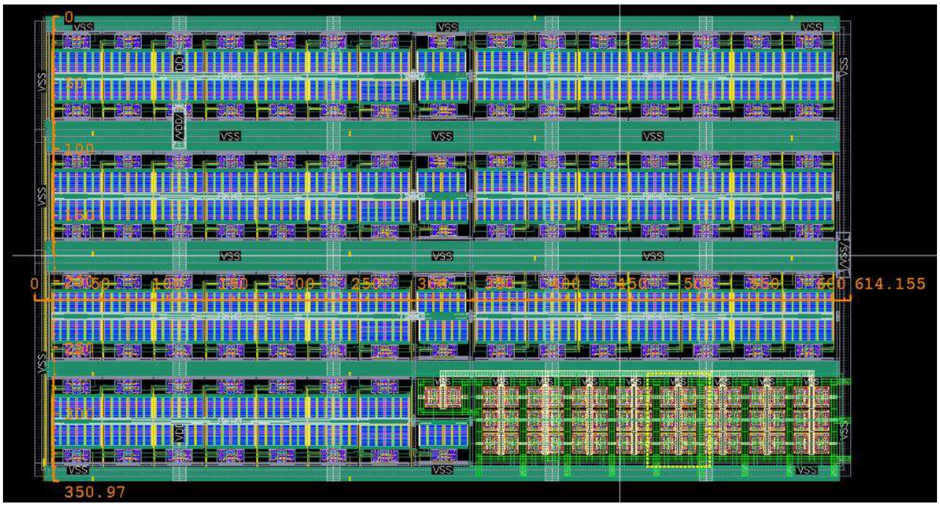

Figure 28. Layout design of the implemented tetrapolar bioimpedance measurement.

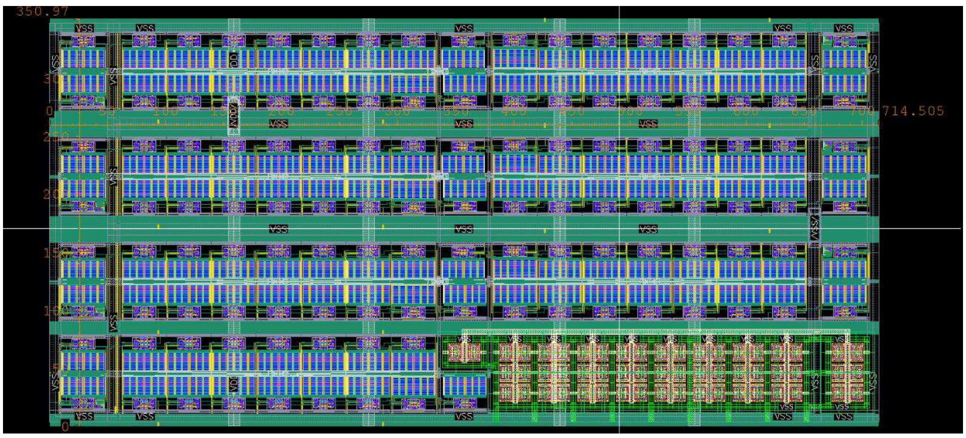

Figure 29. Layout design of the implemented tetrapolar bioimpedance measurement.

4.1. Case I: Balanced Contact Impedances

In this case, all gap resistors are kept at $R_\infty = 1.5$ kΩ, which is a usual medium frequency contact value [61,62]. The target impedances are set to R_b = 100 Ω, 1 kΩ, and 10 kΩ, respectively, so as to model the measurement effect at different orders of magnitude. The 3 subcases are compared with the approximation RC network cases that correspond to a completely passive model.

The results in Figure 30 indicate a maximum magnitude error of 200 Ω and 2° (for the 10 kΩ target case), for both IFLF and versatile methodologies, when compared with the RC network approximation. In addition, it seems that lower absolute impedances (that are usual when measuring with electrodes placed near to each other) can be accurately measured at frequencies near 10 kHz, while higher valued tissue impedance measurements, such as bones, are strongly affected by the presence of skin. The latter therefore needs either invasive techniques or compensation and proper mathematical processing along with the estimated neighboring skin tissue's impedance to be measured at higher frequencies.

4.2. Case II: Imbalanced Contact Impedances

In bio-impedance measuring setups that include multiple electrodes, deviations between the electrode contact impedances is a usual case. These imbalances might be caused by different pressures on each electrode, local differences of the skin surface smoothness, or other external factors that in extreme conditions might lead even to electrode disconnections.

To examine this effect here, we assume 3 fixed electrode gap impedances of $R_{\infty,e} = 1.5$ kΩ, while one of them (in series with the positive voltage acquisition electrode) deviates between the following values: $R_{re} = 500$ Ω, 1 kΩ, 1.5 kΩ, 2.5 kΩ. The target impedance is kept at $R_b = 1$ kΩ. The magnitude and phase results are shown in Figure 31 for versatile design methodology and in Figure 32 for IFLF design methodology. It is shown that, for deviations up to 1 kΩ in contact impedance, we get a maximum magnitude error of 40 Ω and less than 1° of phase error. The choice of IC design methodology does not show effects on the contact impedance's deviation effect in the measurements.

The sensitivity behavior has been evaluated using the Monte-Carlo analysis tool for $N = 100$ runs. The corresponding histograms for impedance and phase for target impedance $R_b = 100$ Ω are demonstrated in Figure 33 for versatile design methodology and in Figure 34 for IFLF design methodology. The mean values of the magnitude and phase for versatile design methodology are $M_{mean} = 95.82$ Ω and $P_{mean} = -1.93°$, and the standard deviations are $\sigma_m = 1.54$ Ω and $\sigma_P = 0.53°$ at $f_o = 1$ kHz, respectively. The mean values of the magnitude and phase for IFLF design methodology are $M_{mean} = 95.69$ Ω and $P_{mean} = -1.96°$, and the standard deviations are $\sigma_m = 1.47$Ω and $\sigma_P = 0.47°$ at $f_o = 1$ kHz, respectively.

The sensitivity behavior has been evaluated using the Monte-Carlo analysis tool for $N = 100$ runs. The corresponding histograms for impedance and phase for target impedance $R_b = 10$ kΩ are demonstrated in Figure 35 for versatile design methodology and in Figure 36 for IFLF design methodology. The mean values of the magnitude and phase for versatile design methodology are $M_{mean} = 9.72$ kΩ and $P_{mean} = -5.52°$, and the standard deviations are $\sigma_m = 0.51$ kΩ and $\sigma_P = 0.71°$ at $f_o = 10$ Hz, respectively. The mean values of the magnitude and phase for IFLF design methodology are $M_{mean} = 9.81$ kΩ and $P_{mean} = -5.64°$, and the standard deviations are $\sigma_m = 0.58$ kΩ and $\sigma_P = 0.61°$ at $f_o = 10$ Hz, respectively.

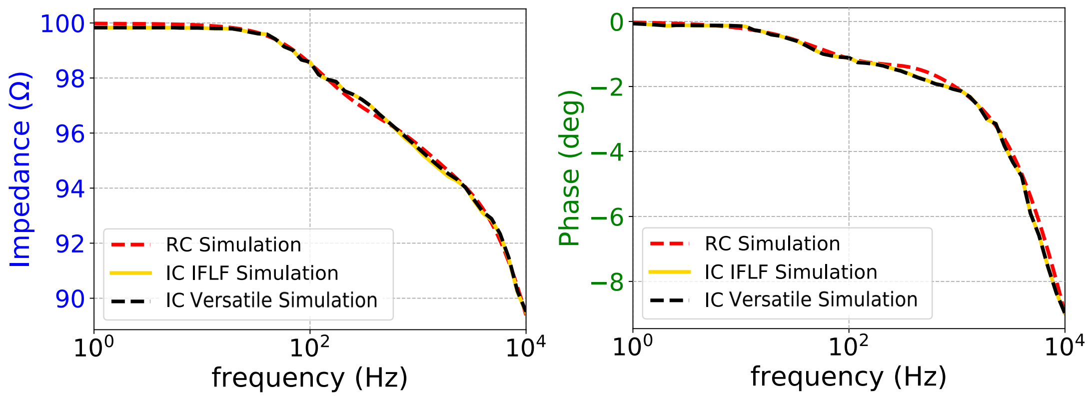

(**a**) $R_b = 100\ \Omega$

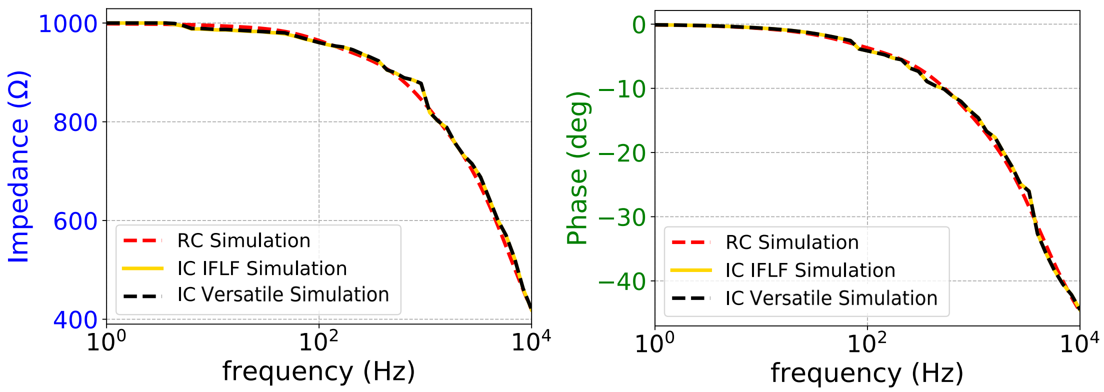

(**b**) $R_b = 1\ \mathrm{k}\Omega$

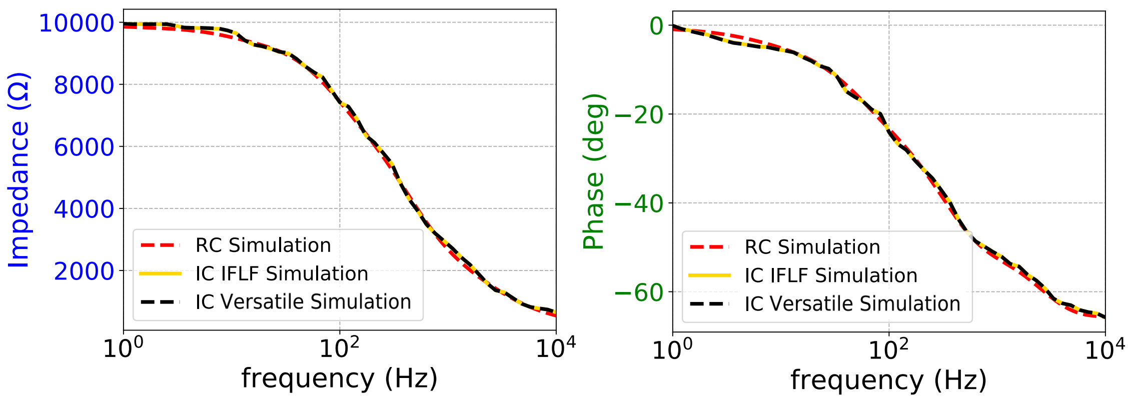

(**c**) $R_b = 10\ \mathrm{k}\Omega$

Figure 30. AC magnitude and phase impedance measurements for (**a**) $R_b = 100\ \Omega$, (**b**) $R_b = 1\ \mathrm{k}\Omega$, and (**c**) $R_b = 10\ \mathrm{k}\Omega$: all electrode and contact impedances are equal ($R_\infty = 1.5\ \mathrm{k}\Omega$). The corresponding RC network approximations are included for comparison.

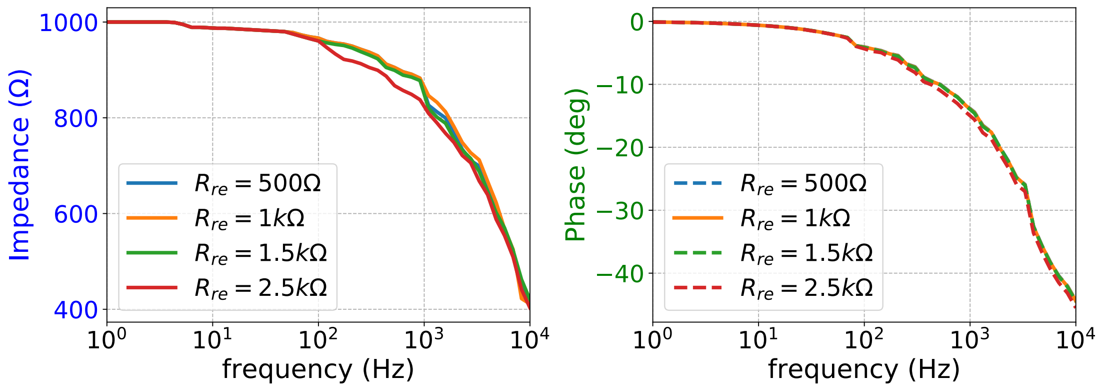

Figure 31. AC magnitude (**left**) and phase (**right**) impedance measurements for deviated shunt impedance of the positive voltage electrode (versatile design).

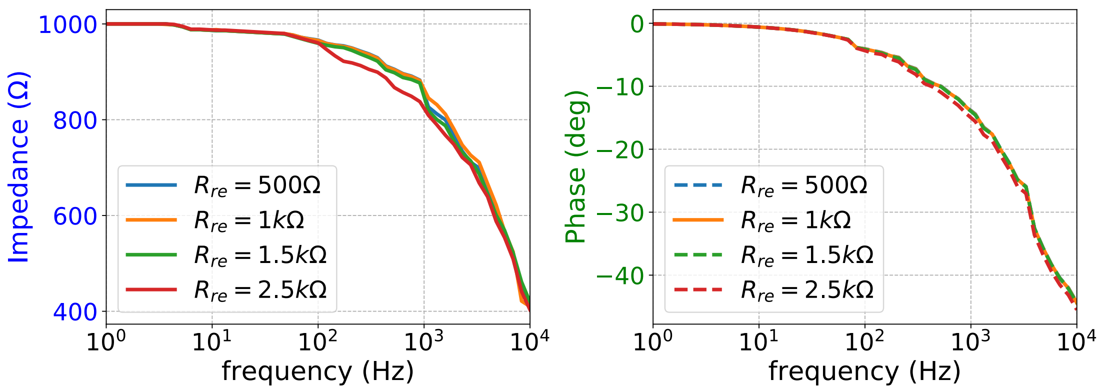

Figure 32. AC magnitude (**left**) and phase (**right**) impedance measurements for deviated shunt impedance of the positive voltage electrode (IFLF design).

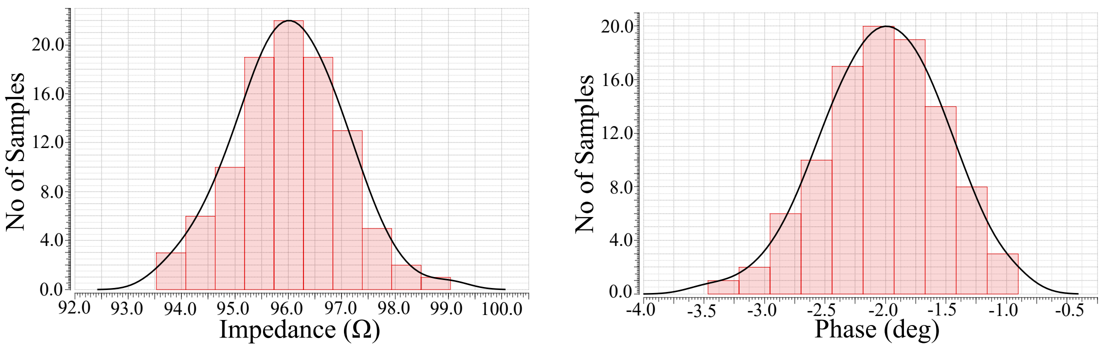

Figure 33. Sensitivity performance of magnitude for target impedance $R_b = 100\ \Omega$ using Monte-Carlo analysis (versatile design).

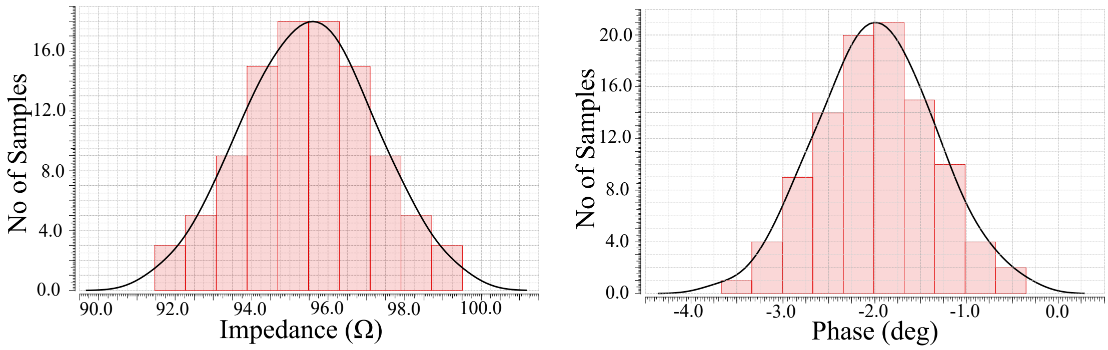

Figure 34. Sensitivity performance of magnitude for target impedance $R_b = 100\ \Omega$ using Monte-Carlo analysis (IFLF design).

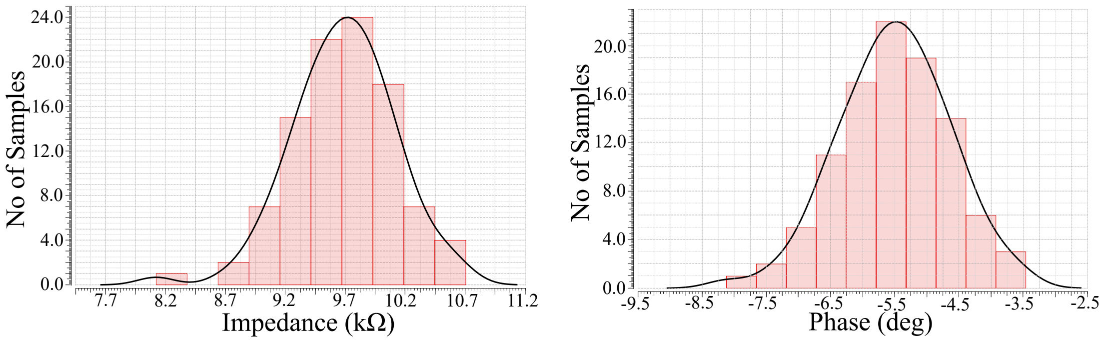

Figure 35. Sensitivity performance of magnitude for target impedance $R_b = 10\ \text{k}\Omega$ using Monte-Carlo analysis (versatile design).

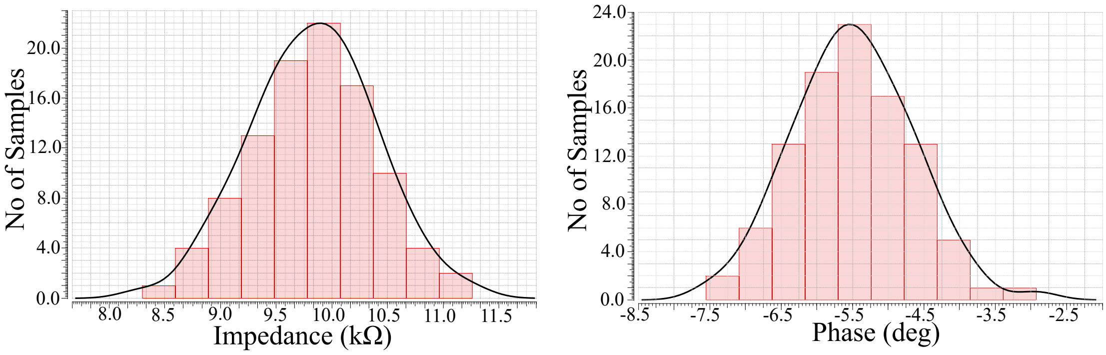

Figure 36. Sensitivity performance of phase for target impedance $R_b = 10\ \text{k}\Omega$ using Monte-Carlo analysis (versatile design).

5. Conclusions

In this paper, we implemented in ASIC architecture the fractional order skin and electrode Cole models following two design methodologies using OTAs and CCIIs as structural elements. Simulation showed very low magnitude and phase errors, while tetrapolar setup simulations revealed possible bio-impedance measuring issues related to the electrode and adjacent skin tissues up to 10 kHz. The ASIC architecture can be used in more complex circuitry setups for calibration and phantom experimental testing more effectively than simple fixed RC networks that are currently used, since they offer sufficient tunability over all frequencies of interest and model parameter variations.

Author Contributions: Investigation, V.A, C.D., and G.P.; writing—original draft, V.A. and C.D.; writing—review and editing, V.A., C.D., and P.P.S. All authors have read and agreed to the published version of the manuscript.

Funding: This research is cofinanced by Greece and the European Union (European Social Fund (ESF)) through the Operational Programme "Human +Resources Development, Education, and Lifelong Learning" in the context of the project "Strengthening Human Resources Research Potential via Doctorate Research" (MIS-5000432), implemented by the State Scholarships Foundation (IKY).

Acknowledgments: The authors would like to thank Ioannis Georgakopoulos for his contribution in the text-editing.

Conflicts of Interest: The authors declare no conflict of interest.

References

1. Gabriel, S.; Gabriel, C.; Corthout, E. The dielectric properties of biological tissues: I. Literature survey. *Phys. Med. Biol.* **1996**, *68*, 2231. [CrossRef]
2. Gabriel, S.; Lau, R.; Gabriel, C. The dielectric properties of biological tissues: II. Measurements in the frequency range 10 Hz to 20 GHz. *Phys. Med. Biol.* **1996**, *41*, 2251. [CrossRef]
3. Gabriel, S.; Lau, R.; Gabriel, C. The dielectric properties of biological tissues: III. parametric models for the dielectric spectrum of tissues. *Phys. Med. Biol.* **1996**, *41*, 2271. [CrossRef]
4. Ibrahim, B.; Jafari, R. Cuffless blood pressure monitoring from an array of wrist bio-impedance sensors using subject-specific regression models: Proof of concept. *IEEE Trans. Biomed. Circuits And Syst.* **2019**, *13*, 1723–1735. [CrossRef] [PubMed]
5. Ibrahim, B.; Hall, D.A.; Jafari, R. Bio-impedance simulation platform using 3D time-varying impedance grid for arterial pulse wave modeling. In Proceedings of the 2019 IEEE Biomedical Circuits and Systems Conference (BioCAS), Nara, Japan, 17–19 October 2019.
6. Adler, A.; Boyle, A. Electrical Impedance Tomography: Tissue Properties to Image Measures. *IEEE Trans. Biomed. Eng.* **2017**, *64*, 11.
7. Mellenthin, M.; Mueller, J.; de Camargo, E.D.; de Moura, F.S.; Santos, T.B.; Lima, R.G.; Hamilton, S.J.; Muller, P.; Alsaker, M. The ACE1 Electrical Impedance Tomography System for Thoracic Imaging. *IEEE Trans. Instrum. Meas.* **2019**, *68*, 3137–3150. [CrossRef]
8. Kassanos, P.; Ip, M.; Yang, G.-Z. A tetrapolar bio-impedance sensing system for gastrointestinal tract monitoring. In Proceedings of the 2015 IEEE 12th International Conference on Wearable and Implantable Body Sensor Networks (BSN), Cambridge, MA, USA, 9–12 June 2015.
9. Ragheb, A.O.; Geddes, L.A.; Bourland, J.D.; Tacker, W.A. Tetrapolar electrode system for measuring physiological events by impedance. *Med. Biol. Eng. Comput.* **1992**, *30*, 115–117. [CrossRef] [PubMed]
10. Brown, B.H.; Wilson, A.J.; Bourland, J.D.; Bertemes-Filho, P. Bipolar and tetrapolar transfer impedance measurements from volume conductor. *Electron. Lett.* **2000**, *36*, 2060–2062. [CrossRef]
11. Simini, F.; Pedro Bertemes-Filho, P. *Bioimpedance in Biomedical Applications and Research*; Springer: New York, NY, USA, 2018.
12. Hanbin, M.; Su, Y.; Nathan, A. Cell constant studies of bipolar and tetrapolar electrode systems for impedance measuremens. *Sens. Actuators B Chem.* **2015**, *221*, 1264–1270.
13. Cardu, R.; Leong, P.H.; Jin, C.T.; McEwan, A. Electrode contact impedance sensitivity to variations in geometry. *Physiol. Meas.* **2012**, *33*, 817. [CrossRef]
14. Chi, Y.M.; Jung, T.-P.; Cauwenberghs, G. Dry-contact and noncontact biopotential electrodes: Methodological review. *IEEE Rev. Biomed. Eng.* **2010**, *3*, 106–119. [CrossRef] [PubMed]
15. Albulbul, A. Evaluating major electrode types for idle biological signal measurements for modern medical technology. *MDPI Bioeng.* **2016**, *3*, 20. [CrossRef] [PubMed]
16. Taji, B.; Chan, A.D.; Shirmohammadi, S. Effect of pressure on skin-electrode impedance in wearable biomedical measurement devices. *IEEE Trans. Instrum. Meas.* **2018**, *67*, 1900–1912. [CrossRef]
17. Grimnes, S.; Martinsen, Ø.G. Sources of error in tetrapolar impedance measurements on biomaterials and other ionic conductors. *J. Phys. D Appl. Phys.* **2006**, *40*, 9. [CrossRef]

18. Kassanos, P.; Demosthenous, A.; Bayford, R.H. Comparison of tetrapolar injection-measurement techniques for coplanar affinity-based impedimetric immunosensors. In Proceedings of the 2008 IEEE Biomedical Circuits and Systems Conference (BioCAS), Baltimore, MD, USA, 20–22 November 2008.
19. Kauppinen, P.; Hyttinen, J.; Malmivuo, J. Sensitivity distribution visualizations of impedance tomography measurement strategies. *Int. J. Bioelectromagn.* **2006**, *8*, 1–9.
20. Shuvo, O.I.; Islam, M.N. Sensitivity Analysis of the Tetrapolar Electrical Impedance Measurement Systems Using COMSOL Multiphysics for the non-uniform and Inhomogeneous Medium. *Dhaka Univ. J. Sci.* **2016**, *64*, 7–13. [CrossRef]
21. Shi, X.; Li, W.; You, F.; Huo, X.; Xu, C.; Ji, Z.; Liu, R.; Li, Y.; Fu, F. High-precision electrical impedance tomography data acquisition system for brain imaging. *IEEE Sens. J.* **2018**, *18*, 5974–5984. [CrossRef]
22. Dimas, C.; Uzunoglu, N.; Sotiriadis, P.P. A Parametric EIT System Spice Simulation with Phantom Equivalent Circuits. *MDPI Technol.* **2020**, *8*, 13. [CrossRef]
23. Dimas, C.; Alimisis, V.; Sotiriadis, P.P. SPICE and MATLAB simulation and evaluation of Electrical Impedance Tomography readout chain using phantom equivalents. In Proceedings of the 2020 European Conference on Circuit Theory and Design (ECCTD), Sofia, Bulgaria, 7–10 September 2020; pp. 1–4. [CrossRef]
24. Wu, Y.; Jiang, D.; Bardill, A.; Bayford, R.; Demosthenous, A. A 122 fps, 1 MHz bandwidth multi-frequency wearable EIT belt featuring novel active electrode architecture for neonatal thorax vital sign monitoring. *IEEE Trans. Biomed. Circuits Syst.* **2019**, *13*, 927–937. [CrossRef]
25. Cole, K.S. Permeability and impermeability of cell membranes for ions. *Cold Spring Harb. Symp. Quant. Biol.* **1940**, *8*, 110–122. [CrossRef]
26. Grimnes, S.; Jiang, D.; Martinsen, O.G. Cole electrical impedance model-a critique and an alternative. *IEEE Trans. Biomed. Eng.* **2004**, *52*, 132–135. [CrossRef]
27. Grimnes, S.; Martinsen, O.G. *Bioimpedance and Bioelectricity Basics*; Academic Press: Cambridge, MA, USA, 2011.
28. Magin, R.L. Fractional calculus in bioengineering. *Begell House Redd.* **2006**, *2*, 6.
29. AboBakr, A.; Said, L.A.; Madian, A.H.; Elwakil, A.S.; Radwan, A.G. Experimental comparison of integer/fractional-order electrical models of plant. *AEU Int. J. Electron. Commun.* **2017**, *80*, 1–9. [CrossRef]
30. Freeborn, T.J. A survey of fractional-order circuit models for biology and biomedicine. *IEEE J. Emerg. Sel. Top. Circuits Syst.* **2013**, *3*, 416–424. [CrossRef]
31. Lazovic, G.; Vosika, Z.; Lazarevic, M.; Simic-Krstic, J.B.; Koruga, D. Modeling of bioimpedance for human skin based on fractional distributed-order modified cole model. *FME Trans.* **2014**, *42*, 74–81. [CrossRef]
32. Vosika, Z.; Lazovic, G.; Misevic, G.M.; Simic-Krstic, J.B. Fractional calculus model of electrical impedance applied to human skin. *PLoS ONE* **2013**, *8*, 4. [CrossRef]
33. Poon, C.; Choy, T. Frequency dispersions of human skin dielectrics. *Biophys. J.* **1981**, *34*, 135–147. [CrossRef]
34. Eggins, B.R. Skin contact electrodes for medical applications. *Analyst* **1993**, *118*, 439–442. [CrossRef] [PubMed]
35. Goren, N.; Avery, J.; Dowrick, T.; Mackle, E.; Witkowska-Wrobel, A.; Werring, D.; Holder, D. Multi-frequency electrical impedance tomography and neuroimaging data in stroke patients. *Sci. Data Nat.* **2018**, *5*, 1801–1812. [CrossRef]
36. Rao, A.; Murphy, E.; Halter, R.; Odame, K. A 1 MHz Miniaturized Electrical Impedance Tomography System for Prostate Imaging. *IEEE Trans. Biomed. Circuits Syst.* **2020**, *14*, 787–799. [CrossRef]
37. Alimisis, V.; Pappas, G.; Sotiriadis, P. Fractional-Order Instrumentation Amplifier Transfer Function for Control Applications. In Proceedings of the 33rd Symposium on Integrated Circuits and Systems Design, Campinas, Brazil, 24–28 August 2020.
38. Tsirimokou, G.; Psychalinos, C.; Freeborn, T.; Elwakil, A. Emulation of current excited fractional-order capacitors and inductors using OTA topologies. *Microelectron. J.* **2016**, *55*, 70–81. [CrossRef]
39. Vastarouchas, C.; Tsirimokou, G.; Freeborn, T.J.; Psychalinos, C. Emulation of an electrical-analogue of a fractional-order human respiratory mechanical impedance modelusing OTA topologies. *Int. J. Electron. Commun. (AEU)* **2017**, *78*, 201–208. [CrossRef]
40. Tsirimokou, G.; Psychalinos, C.; Elwakil, A. Emulation of a Constant Phase Element Using Operational Transconductance Amplifiers. *Analog. Integr. Circuits Signal Process.* **2015**, *85*, 413–423. [CrossRef]

41. Tsirimokou, G.; Kartci, A.; Koton, J.; Herencsar, N.; Psychalinos, C. Comparative Study of Discrete Component Realizations of Fractional-Order Capacitor and Inductor Active Emulators. *J. Circuits Syst. Comput.* **2017**, *27*, 11. [CrossRef]
42. Papachristopoulou, Z.; Kapoulea, S.; Psychalinos, C.; Elwakil, A.S. Design of Fractional-Order Emulator of the Cardiac Tissue Electrode Interface. In Proceedings of the 42nd International Conference on Telecommunications and Signal Processing (TSP), Budapest, Hungary, 1–3 July 2019.
43. Vastarouchas, C.; Psychalinos, C.; Elwakil, A.S. Fractional-order model of a commercial ear simulator. In Proceedings of the 2018 IEEE International Symposium on Circuits and Systems (ISCAS), Florence, Italy, 27–30 May 2018.
44. Baxevanaki, K.; Psychalinos, C. Second-Order Bandpass OTA-C Filter Designs for Extracting Waves from Electroencephalogram. In Proceedings of the 8th International Conference on Modern Circuits and Systems Technologies, Thessaloniki, Greece, 13–15 May 2019.
45. Alimisis, V.; Bertsias, P.; Psychalinos, C.; Elwakil, A.S. Electronically tunable implementation of the arterial viscoelasticity model. In Proceedings of the 42nd International Conference on Telecommunications and Signal Processing (TSP), Budapest, Hungary, 1–3 July 2019.
46. Alimisis, V.; Gourdouparis, M.; Dimas, C.; Sotiriadis, P.P. Implementation of Fractional-order Model of Nickel-Cadmium Cell using Current Feedback Operational Amplifiers. In Proceedings of the 2020 European Conference on Circuit Theory and Design (ECCTD), Sofia, Bulgaria, 7–10 September 2020; pp. 1–4. [CrossRef]
47. Valsa, J.; Vlach, J. RC models of a constant phase element. *Int. J. Circuit Theory Appl.* **2013**, *41*, 59–67. [CrossRef]
48. Tsirimokou, G. A systematic procedure for deriving RC networks of fractional-order elements emulators using MATLAB. *AEU Int. J. Electron. Commun.* **2017**, *78*, 7–14. [CrossRef]
49. Psychalinos, C.; Elwakil, A.; Maundy, B.; Allagui, A. Analysis and realization of a switched fractional-order-capacitor integrator. *Int. J. Circuit Theory Appl.* **2016**, *44*, 2035–2040. [CrossRef]
50. Tsirimokou, G.; Psychalinos, C.; Elwakil, A.; Salama, K.N. Experimental Verification of on Chip CMOS Fractional-Order Capacitor Emulators. *IET Electron. Lett.* **2016**, *52*, 1298–1300. [CrossRef]
51. Dimeas, I.; Tsirimokou, G.; Psychalinos, C.; Elwakil, A. Experimental Verification of Fractional-Order Filters Using a Reconfigurable Fractional-Order Impedance Emulator. *J. Circuits Syst. Comput.* **2017**, *26*, 9. [CrossRef]
52. Bertsias, P.; Psychalinos, C.; Elwakil, A.; Maundy, B. Current-Mode Capacitorless Integrators and Differentiators for Implementing Emulators of Fractional-Order Elements. *Int. J. Electron. Commun. (AEU)* **2017**, *80*, 94–103. [CrossRef]
53. Domansky, O.; Sotner, R.; Langhammer, L.; Jerabek, J.; Psychalinos, C.; Tsirimokou, G. Practical Design of Constant Phase Elements and Their Implementation in Fractional-Order PID Regulators Using CMOS Voltage Differencing Current Conveyors. *Circuits Syst. Signal Process.* **2018**, *38*, 4. [CrossRef]
54. Kapoulea, S.; Psychalinos, C.; Elwakil, A. Single active element implementation of fractional-order differentiators and integrators. *Int. J. Electron. Commun. (AEU)* **2018**, *97*, 6–15. [CrossRef]
55. Bertsias, P.; Psychalinos, C.; Maundy, B.; Elwakil, A.S.; Radwan, A. Partial Fraction Expansion Based Realizations of Fractional-Order Differentiators and Integrators Using Active Filters. *Int. J. Circuit Theory Appl.* **2019**, *47*, 513–531. [CrossRef]
56. Kapoulea, S.; Psychalinos, C.; Elwakil, A. Realizations of Simple Fractional-Order Capacitor Emulators with Electronically-Tunable Capacitance. *Integration* **2019**, *69*, 225–233. [CrossRef]
57. Kaskouta, E.; Kapoulea, S.; Psychalinos, C.; Elwakil, A. Implementation of a Fractional-Order Electronically Reconfigurable Lung Impedance Emulator of the Human Respiratory Tree. *J. Low Power Electron. Appl.* **2020**, *10*, 18. [CrossRef]
58. Kapoulea, S.; Psychalinos, C.; Elwakil, A. Double Exponent Fractional-Order Filters: Approximation Methods and Realization. *Circuits Syst. Signal Process.* **2020**, 1–12. [CrossRef]
59. Tsirimokou, G.; Psychalinos, C.; Elwakil, A.S. *Design of CMOS Analog Integrated Fractional-Order Circuits: Applications in Medicine and Biology*; Springer: Berlin/Heidelberg, Germany, 2017.
60. Dimeas, I.; Petras, I.; Psychalinos, C. New analog implementation technique for fractional-order controller: A DC motor control. *AEU Int. J. Electron. Commun.* **2017**, *78*, 192–200. [CrossRef]

61. Kusche, R.; Kaufmann, S.; Ryschka, M. Dry electrodes for bioimpedance measurements—Design, characterization and comparison. *Biomed. Phys. Eng. Express* **2018**, *5*, 015001. [CrossRef]
62. Isik, M.; Lonjaret, T.; Sardon, H.; Marcilla, R.; Herve, T.; Malliaras, G.G.; Ismailova, E.; Mecerreyes, D. Cholinium-based ion gels as solid electrolytes for long-term cutaneous electrophysiology. *J. Mater. C* **2015**, *3*, 8942–8948. [CrossRef]